



Changes in antimony isotopic composition as a tracer of hydrothermal fluid evolution at the Sb deposits in Pezinok (Slovakia)

Andreas B. Kaufmann^{1,2} · Marina Lazarov² · Stefan Weyer² · Martin Števkó^{3,4} · Stefan Kiefer¹ · Juraj Majzlan¹

Received: 22 June 2023 / Accepted: 30 September 2023
© The Author(s) 2023

Abstract

In this work, we investigated in situ isotopic compositions of antimony (Sb) minerals from two substages of the ore deposits near Pezinok (Slovakia). The $\delta^{123}\text{Sb}$ values of the primary Sb minerals range from -0.4 and $+0.8\text{‰}$ and increase progressively along the precipitation sequence. In the substage II, the early-formed gudmundite (FeSbS) shows in all sections the lowest $\delta^{123}\text{Sb}$ values, followed by berthierite (FeSb_2S_4), stibnite (Sb_2S_3), and valentinite (Sb_2O_3) with the heaviest $\delta^{123}\text{Sb}$ values. A similar trend was observed for the substage III, from the initially-formed stibnite, followed by kermesite ($\text{Sb}_2\text{S}_2\text{O}$), valentinite, senarmontite (both Sb_2O_3), and schafarzikite (FeSb_2O_4). The evolution can be rationalized by a Rayleigh fractionation model with a starting $\delta^{123}\text{Sb}$ value in the fluid of $+0.3\text{‰}$, applying the same mineral-fluid fractionation factor to all minerals. Thus, the texturally observed order of mineralization is confirmed by diminishing trace element contents and heavier $\delta^{123}\text{Sb}$ values in successively crystallized Sb minerals. Antimony in substage III was likely supplied from the oxidative dissolution of stibnite that formed earlier during substage II. The data interpretation, although limited by the lack of reliable mineral-fluid fractionation factors, implies that Sb precipitation within each substage occurred from an episodic metal precipitation, likely associated with a similar Sb isotope fractionation between fluid and all investigated Sb minerals. Large isotopic variations, induced by precipitation from a fluid as a response to temperature decrease, may be an obstacle in deciphering the metal source in hydrothermal ore deposits. However, Sb isotopes appear to be an excellent instrument to enhance our understanding on how hydrothermal systems operate.

Keywords Antimony isotopes · Sb sulfides and oxides · Rayleigh fractionation · Ore deposit · Pezinok · Precipitation sequence

Editorial handling: D. Zhai

✉ Andreas B. Kaufmann
a.kaufmann@mineralogie.uni-hannover.de

¹ Institute of Geosciences, Friedrich Schiller University Jena, Jena, Germany

² Institute of Mineralogy, Leibniz University Hannover, Hannover, Germany

³ Earth Science Institute v.v.i., Slovak Academy of Sciences, Dúbravská cesta 9, P. O. BOX 106, 840 05 Bratislava, Slovakia

⁴ Department of Mineralogy and Petrology, National Museum, Cirkusová 1740, 193 00 Prague9, Horní Počernice, Czech Republic

Introduction

Precipitation of antimony and formation of Sb ore deposits is generally related to low-temperature ($< 250\text{ °C}$) hydrothermal fluids of metamorphic or magmatic origin (Sillitoe and Hedenquist 2005; Dill et al. 2008; Li and Audétat 2012; Helmy et al. 2010; Spiridonov et al. 2015; Burisch et al. 2019). A direct link to the Sb source can only be deduced for some hydrothermal mineralizations (Goldfarb and Pitcairn 2023). Antimony minerals are often accompanied by minerals of other elements and there may be multiple sources of the different elements (Patten et al. 2023). The largest Sb reserves are linked to orogenic deposits, related to mid- or lower-crustal metamorphism or igneous activity (Kretschmar and McBride 2016; Goldfarb and Pitcairn 2023). These deposits may form from fluids that circulate in the deeper crustal sections and deposit their metal load far away from the original source. Thus, the formation

of these ore deposits, including the source of the fluids, of the metals and metalloids, as well as the precipitation mechanisms, is difficult to elaborate (Riddley 2013; Robb 2020). Mineral associations in all Sb ore deposits are dominated by stibnite (Sb_2S_3) and rarely accompanied by a number of Pb-Fe-Sb phases (e.g., berthierite, gudmundite, and jamesonite), Pb-Sb sulfosalts (e.g., zinkenite and boulangerite), or Cu-Sb minerals (e.g., tetrahedrite, chalcostibite, and bournonite) (Majzlan 2021). The mineralogical variability of the Sb minerals in some of these deposits and their Sb isotopic variations could constitute a novel tracer to constrain the mechanisms of Sb ore formation. This effort parallels the increasing use of other stable isotope systems, such as Fe (e.g., Wang et al. 2011, 2015; Xu et al. 2020; Pokrovski et al. 2021), Cu (e.g., Graham et al. 2004; Gregory and Mathur 2017; Zhao et al. 2022), Zn (e.g., Mason et al. 2005; Wilkinson et al. 2005; Matt et al. 2022), or other heavier elements to explore the formation of ore deposits.

Stable isotopes of antimony (^{121}Sb and ^{123}Sb) display a variation of $\delta^{123}\text{Sb}$ values of around 2‰ (Wen et al. 2018). To date, most Sb isotope studies focused on the optimization of Sb isotope analyses of purified solutions with MC-ICP-MS (e.g., Rouxel et al. 2003; Lobo et al. 2012; Liu et al. 2020; Ferrari et al. 2021; Li et al. 2021; Sun et al. 2021; Fang et al. 2022). Most studies on ore minerals focused on bulk measurements of stibnite (Tanimizu et al. 2011; Lobo et al. 2012; Degryse et al. 2020) and observed a range of 1‰ in the $\delta^{123}\text{Sb}$ values. Zhai et al. (2021) used Sb isotopes to address the directionality of the fluid flow during the ore-formation process and estimated for the first time an Sb isotope fractionation factor in the system stibnite fluid. Wang et al. (2021) discussed the first example of a redox-controlled Sb isotope fractionation in an epithermal system, whereas Yu et al. (2022) showed the effect of the Sb speciation change in the fluid from $\text{H}_2\text{Sb}_2\text{S}_4$ to $\text{Sb}_2\text{S}_2(\text{OH})_2$ on Sb isotopic fractionation. Apart from addressing the formation of primary hydrothermal ores, studies with environmental focus (Tanimizu et al. 2011; Resongles et al. 2015; Wen et al. 2023) used Sb isotopes to elucidate the source and mobilization processes in mine-affected water systems. Araki et al. (2009), Wasserman et al. (2019), Zhou et al. (2022), and Zhou et al. (2023) described Sb isotope fractionation during the adsorption of Sb onto solid substrates. Using density-functional theory, Ferrari et al. (2022) predicted the magnitude of equilibrium isotopic fractionation during the transition from Sb sulfide to Sb oxide. A new in situ method for the measurements of Sb isotopes with femtosecond laser ablation (LA) multicollector (MC)-ICP-MS (Kaufmann et al. 2021) showed $\delta^{123}\text{Sb}$ variations of up to 1.4‰ at the micrometer scale in Sb sulfides, oxides, and sulfosalts. The authors proved the accuracy of their method by comparative isotope measurements on a number of Sb minerals (senarmontite, chalcostibite, tetrahedrite, boulangerite, and pyrargyrite) using both solution and LA-MC-ICP-MS. This method provides the means to extend

the use of the Sb isotopes to investigate minerals other than stibnite in ore deposits.

Here, we present textural relationships, trace element, and in situ antimony isotopic composition of a suite of primary minerals, including native antimony, sulfantimonides, Sb sulfides, sulfoxides, and oxides from a deposit camp between Pezinok and Pernek in the Western Carpathians in Slovakia. These deposits are a model system with several stages of mineral evolution, from highly reduced assemblages, through the main mass of stibnite, to a late, oxidized hydrothermal assemblage (Chovan et al. 1994; Majzlan et al. 2020a and references therein). Due to the presence of several stages of mineral evolution, the mineral textures in individual sections may be complex. Thus, in situ Sb isotope data in conjunction with trace element composition and mineralogical textural observations for the deposit camp near Pezinok represent an ideal case study for the evolution of a hydrothermal Sb ore deposit.

Regional geological setting and mineralization

The Western Carpathians (WC) are a part of the European Alpides (Fig. 1, Plašienka 2018). They are made of (1) fragments of Early Paleozoic basement intruded by Variscan granitoids, (2) late Paleozoic to Mesozoic autochthonous and allochthonous sedimentary cover, and (3) Mesozoic, Paleogene, and Neogene sediments and volcanic rocks. The Kolársky vrch, Trojárová, and Pernek-Křížnica ore deposits near Pezinok are located in the Tatric Superunit of the Central Western Carpathians (CWC), in the Malé Karpaty Mountains, the westernmost fragment of CWC (Fig. 1). Several superposed Alpine nappes, consisting of pre-Alpine basement, autochthonous, and subautochthonous Mesozoic cover, and allochthonous higher nappes (Fatric and Hronic Superunit) build the current geological structure of the Malé Karpaty Mts. (Plašienka et al. 1991). The pre-Alpine basement includes two types of granitic rocks (southern Bratislava and northern Modra massifs) and a metamorphic complex between the two granitic massifs. This complex consists of two groups named Pernek and Pezinok group, displaced and brought in tectonic contact in pre-Viséan times (Ivan and Méres 2006). Both groups are stretching in the NW-SE direction and underwent multiple stages of metamorphic overprint, including low-grade regional metamorphism at 380 ± 20 Ma (Cambel et al. 1990) and periplutonic contact metamorphism by the granitic rocks of the Bratislava and Modra massif (355–347 Ma; Kohút et al. 2009). The rocks of the Bratislava massif are represented by peraluminous monzogranites and granodiorites (S-type granites), while the Modra massif is defined by meta-aluminous to peraluminous biotitic granodiorites and tonalites (I-type granite; Kohút et al. 2009).

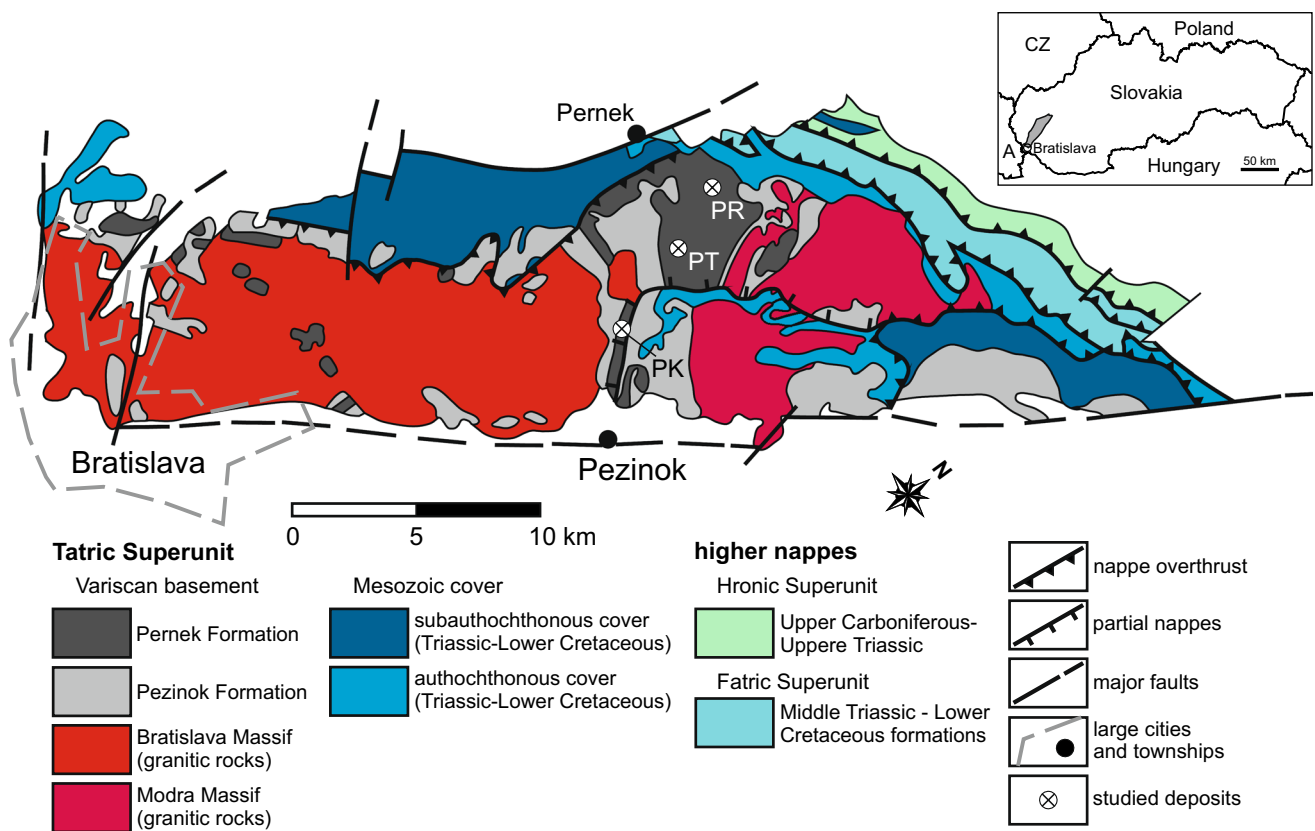


Fig. 1 A simplified geological map of the Malé Karpaty Mts. The inset in the upper right corner shows the position of the map area (gray) in central Europe. The location of the studied deposits is shown: PT, Pezi-

nok-Trojárová; PR, Pernek-Křížnica; PK, Pezinok-Kolársky vrch. Simplified after Plašienka et al. (1991), Chovan et al. (1992), and Ivan and Méres (2006)

Chovan et al. (1992) described in detail the Sb-Au deposits in the Malé Karpaty Mts. which were extensively mined until 1992. The largest deposits in this camp are the deposits Kolársky vrch, Trojárová, and Pernek-Křížnica (Fig. 1). All Sb-Au ores are hosted within the Pernek group, that is considered to represent an incomplete, dismembered, and metamorphosed ophiolite sequence (Ivan and Méres 2006). The most common rocks are metamorphosed basalts and gabbros. The stratigraphically highest rocks in the original sequence are now represented by thin layers of metasilicic rocks with organic admixture (metamorphosed black shales, with 1–8% of non-carbonate C, Chovan et al. 1992) and chlorite-actinolite schists.

The ore mineralization in the studied deposits is bound to lenses of metamorphosed black shales in chlorite-actinolite schists or in gneisses (Fig. 2). At Kolársky vrch, the ore bodies consist of short veinlets, lenses, and incrustations, with a total thickness of up to 30 m at a full length of 300–500 m and a depth of 60–100 m (Cambel 1959). Similarly to Kolársky vrch, the mineralization zone at Trojárová has NW-SE strike with a dip to NE, but the ore bodies are thinner, with a thickness of up to 0.5 m. At Pernek-Křížnica, the metamorphosed black shales reach

a thickness of several meters but the field observations are difficult because only a small portion of the mines is accessible.

Two different types of ore mineralization can be distinguished in all of these three deposits near Pezinok (Chovan et al. 1994): (1) earlier massive sulfides of volcano-sedimentary origin, transformed by the Variscan metamorphism to pyrite-pyrrotite (for the chemical formulae of all minerals mentioned in this text, see Table 1) mineralization and (2) later strata-bound Sb-As-Au mineralization (Chovan et al. 1992; Bukovina 2006; Chovan et al. 2006).

The main focus of this study is the strata-bound Sb-As-Au mineralization whose precipitation sequence and the relative timing of the minerals were investigated by Cambel (1959), Andráš (1983), Chovan et al. (1994), Bukovina (2006), and Chovan et al. (2006). They used spatial and textural relationships among the minerals observed in thin and polished sections, as well as thermodynamic predictions. All these authors agree that the hydrothermal precipitation sequence of all Sb-As-Au deposits in the Malé Karpaty Mts. can be subdivided into three substages.

The first substage (substage I) commenced with quartz and Au-bearing pyrite and arsenopyrite at crystallization

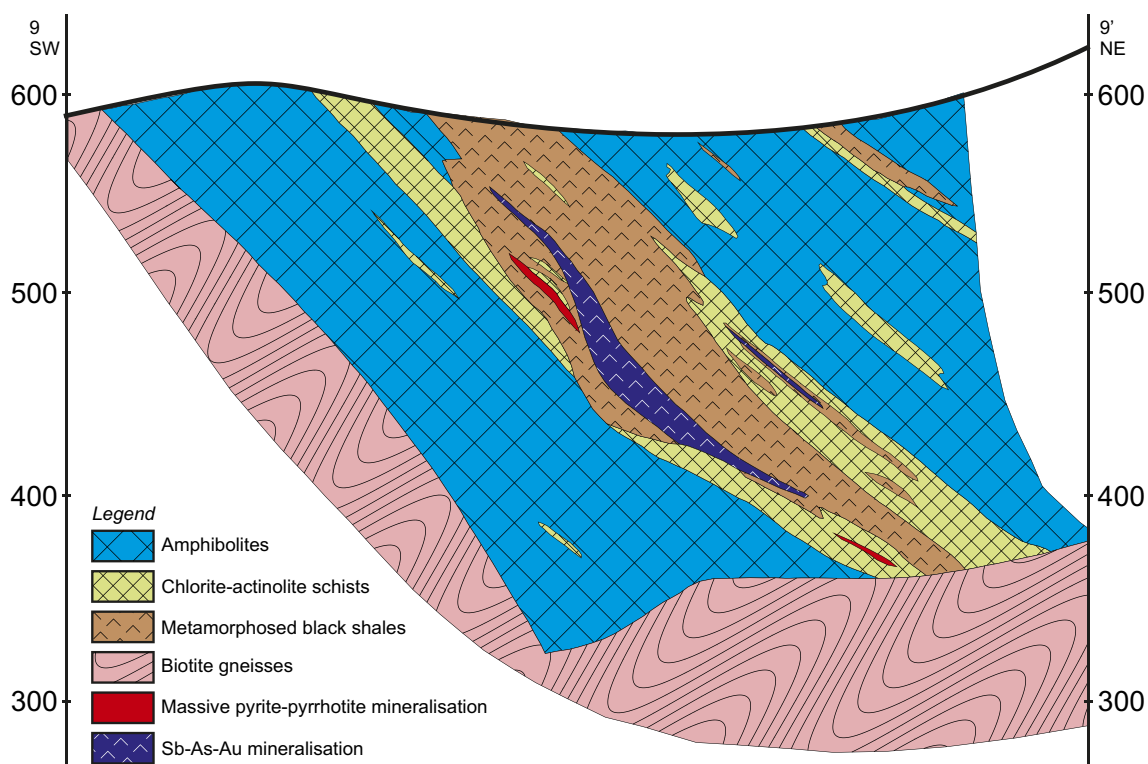


Fig. 2 Geological profile of the deposit Pezinok-Trojárová (after Chovan et al. 1994)

Table 1 Names and chemical formulae of the minerals mentioned in the text

Antimony	Sb	Pyrrhotite	Fe_{1-x}S
Arsenopyrite	FeAsS	Quartz	SiO_2
Barite	BaSO_4	Schafarzikite	FeSb_2O_4
Berthierite	FeSb_2S_4	Senarmontite	Sb_2O_3
Gudmundite	FeSbS	Stibnite	Sb_2S_3
Kermesite	$\text{Sb}_2\text{S}_2\text{O}$	Valentinite	Sb_2O_3
Pyrite	FeS_2		

temperatures of ~ 350 °C (Andráš et al. 2003). These two minerals are accompanied by minor amounts of löllingite, gudmundite, and pyrrhotite, all bound to quartz and carbonate lenses and veins in the metamorphosed black shales and in the chlorite-actinolite schists (Chovan et al. 1992, 2002). Arsenopyrite and pyrite contain invisible gold, with recorded Au concentrations up to 38 ppm (Andráš and Chovan 2001). These minerals were followed by precipitation of quartz-carbonate-stibnite (substage II) with less abundant native antimony, gudmundite, pyrrhotite, berthierite, and valentinite. This stage was the main target of exploitation. The substage III is restricted to a few millimeter-thick fractures that cross-cut the earlier mineralization and is represented by minor stibnite and more abundant valentinite,

senarmontite, schafarzikite, and kermesite. The deposit camp near Pezinok is a prominent example of precipitation of primary hydrothermal Sb sulfoxides and oxides, together with a few other deposits (see Normand et al. 1996). There is no doubt that the oxidic Sb minerals are primary. They form large, well-developed crystals, and may occur together with earlier, massive stibnite in specimens with no signs of weathering. Samples that showed weathering features, such as earthy reddish dusting of secondary kermesite or yellowish crusts of stibiconite, were excluded from this work.

The host rocks of the Sb-Au ores experienced intensive hydrothermal alterations whose nature changes progressively with the distance from the ore bodies (Moravský and Lipka 2004). The innermost carbonatization zone is most intense at the contact between the metamorphosed black shales and the chlorite-actinolite schists and can be observed either in the foliation or in veins cutting the foliation. Illitization is pervasive as illite formed at the expense of plagioclase and chlorites. In a more distant zone, carbonates are still abundant but chlorites are preserved. In the distal zone, carbonates are scarce or missing and chlorite is present. Pyritization and desilicification of the rocks are discernible. Based on estimates of the temperature and chemical composition of the fluids that caused alteration (Moravský and Lipka 2004), the alteration processes can be linked to the formation of the Sb-As-Au mineralization studied in this work.

There are no quantitative data on the Sb reserves in the substage II and substage III. Based on our previous work (Majzlan et al. 2020a), we estimate that the substage II represents well over 90% of the entire Sb budget of the deposit.

In this work, for simplicity, we specify the substage for a mineral with a suffix, for example, stibnite-II for the stibnite that precipitated in substage II.

Analytical procedure

Mineral characterization

Sixty-six samples were collected in the abandoned adits from three studied sites Pezinok-Kolársky vrch (abbreviated as PK), Pezinok-Trojárová (PT), and Pernek-Křížnica (PR). Thin and polished sections of the ore minerals were prepared and examined in reflected polarized light. The ore minerals (Table 1) were investigated for major and minor elements by electron microprobe analyses (EMPA) using a JEOL JXA-8230 at the University of Jena. The measurement conditions of wavelength-dispersive X-ray (WDX) analyses were set to an accelerating voltage of 20 kV, a beam current of 20 nA, and a beam diameter of 1 μm . WDX was used to measure the X-ray lines of the elements S ($\text{K}\alpha$), Fe ($\text{K}\alpha$), Cu ($\text{K}\alpha$), As ($\text{K}\alpha$), Sb ($\text{L}\alpha$), Pb ($\text{M}\alpha$), and Ni ($\text{K}\alpha$). Counting times were set to 40 s to improve count-rate statistics. The standards used for calibration were stibnite for S and Sb, chalcopyrite for Cu, pyrite for Fe, arsenopyrite for As, galena for Pb, and elemental Ni. The detection limits were calculated from the background counts, the measurement time, and the standard material concentration, amount to 0.04 wt.% for S, Ni, and Fe; 0.05 for Cu; 0.06 for As; 0.08 for Sb; and 0.09 for Pb.

Trace element microanalyses

The trace element analyses were carried out in situ using an Element XR (Thermo Scientific, Germany) fast-scanning sector field ICP-MS coupled to a femtosecond laser ablation (fs-LA) system (Solstice, Spectra-Physics, USA) at the Leibniz University Hannover (Germany). Sample ablation was achieved with a deep UV ($\lambda = 194 \text{ nm}$) laser with energy pulses of 70–90 mJ. Analyses were conducted with a laser beam width of 60 μm and a repetition rate of 18 Hz for standards and a 40–60- μm spot size and repetition rate between 16 and 50 Hz for samples. Ablated particles were transported from the sample chamber by He carrier gas and mixed with Ar before entering the Element XR. A Jet sample cone and a skimmer X cone were used (material composed of Ni) in combination with a 1-mm copper ring (spacer). During instrument tuning, the oxide rate formation was optimized to a ThO/Th value $\leq 0.5\%$. The external reference standards were NIST SRM 610 (Jochum et al. 2011) and PGE-A (Gilbert et al. 2013). Depending on the major element composition of the investigated minerals, the Fe, Ni, Cu, or Sb

concentrations determined by EPMA were used for internal standardization. The PGE-A standard was frequently analyzed for quality control. The reproducibility achieved for all trace elements was better than 10% for most elements. Data were reduced and drift corrected, using a MATLAB-based SILLS program (Guillong et al. 2008). Argide interference from $^{67}\text{Zn}^{40}\text{Ar}$ and silver (^{107}Ag) was corrected by measuring sphalerite (ZnS) reference materials. The obtained interference level was proportionally subtracted from the sample, to obtain the argide-free sample concentration.

In situ Sb isotope analyses

In situ Sb isotope analyses were performed using a femtosecond laser ablation system (Solstice, Spectra-Physics, USA) coupled to MC-ICP-MS (Thermo-Scientific Neptune Plus) at the Leibniz University Hannover (Horn and von Blanckenburg 2007; Lazarov and Horn 2015). The analyses were conducted on standard polished sections in accordance with the protocol described in detail by Kaufmann et al. (2021). The instrumental drift correction was applied by sample-standard bracketing and the instrumental mass bias was monitored by simultaneous analyses of a Sn standard solution (NIST SRM 3161a, 1 ppm Sn) (Tanimizu et al. 2011). The Sn standard solution was aspirated at a rate of $\sim 50\text{--}100 \mu\text{l min}^{-1}$ through an ESI PFA-ST nebulizer into a quartz spray chamber. Depending on the mineral grain size and Sb content, spot diameter between 30 and 60 μm and repetition rates between 4 and 25 Hz were applied, to achieve signal intensity comparable to those of the in-house synthetic stibnite standard (labeled SC, see Kaufmann et al. 2021). All in situ Sb isotope analyses were performed using standard-sample bracketing with the SC stibnite in-house standard (Kaufmann et al. 2021). Subsequently, $\delta^{123}\text{Sb}$ values relative to SC stibnite were recalculated and reported relative to the Sb isotope standard NIST SRM 3102a (applying: $\delta^{123}\text{Sb}_{\text{NIST3102a}} = \delta^{123}\text{Sb}_{\text{Sample}} - 0.189\%$; Kaufmann et al. 2021). The in-house Sb standards MAC (stibnite, Micro-Analysis Consultants Ltd. -Stock No: 45464, lot number: L10S026) and MET (metal, Alfa Aesar, lot number: X0034087-1) were repeatedly analyzed over a measurement duration of 3 months. The long-term $\delta^{123}\text{Sb}$ mean values of $0.640 \pm 0.050\%$ (2SD) and $0.210 \pm 0.067\%$ (2SD) obtained for MAC and MET, respectively, relative to NIST SRM 3102a, are in a good agreement with those reported by Kaufmann et al. (2021).

Results

Petrography

The strata-bound Sb-As-Au mineralization is largely restricted to the metamorphosed black shales. When the contacts

between the metamorphosed black shales and the schists or gneisses are observable, the Sb-As-Au mineralization fades out rapidly when leaving the metamorphosed black shales. This situation is observed especially at Kolársky vrch where the bodies of the metamorphosed black shales are thick. There are only thin, submillimeter coatings of stibnite present occasionally on small fractures in the schists or gneisses. At Trojárová, the bodies of the metamorphosed black shales are thinner and there is sporadically rich mineralization also in the nearby chlorite-actinolite schists (Fig. 3a).

The aggregates of the Sb minerals of substage II form lenticular bodies, with or without quartz or Fe-dolomite, that follow the structures developed during the tectonic reworking of the host rocks. The centers of these structures are usually occupied by fine- to medium-crystalline stibnite, sometimes with berthierite. The richest, massive accumulations of stibnite contain also inclusions or aggregates of native antimony. Rims of the lenses contain gudmundite and berthierite (Fig. 3a). At Pernek-Křížnica, the ores are also made mostly of stibnite but the proportion of contemporaneous hydrothermal pyrite is distinctly higher than at Kolársky vrch or Trojárová.

Native antimony occurs as lenses in massive stibnite (Fig. 3b) or microscopically together with gudmundite and stibnite, but also with valentinite (Fig. 3c). Native antimony forms fine-grained aggregates with mosaic textures. Stibnite corrodes and replaces euhedral and subhedral gudmundite crystals (Fig. 3b). Stibnite and berthierite form massive aggregates with mosaic texture and pressure-induced

twinning in the stibnite crystals is common. All sulfides and native antimony are locally replaced by hydrothermal valentinite or senarmontite (Fig. 3c).

The lenses of the metamorphosed black shales are cut by diagonal fractures, mineralized by acicular crystals of stibnite, kermesite, and valentinite (substage III, Fig. 4a, b), with occasional crystals of calcite, barite, and siderite. The deposit Kolársky vrch is known for its primary kermesite crystals which attain a length of 10 cm or even more. At Pernek-Křížnica, schafarzikite is a fairly common late hydrothermal mineral (Fig. 4c), forming crystals in the vugs of Fe-dolomite or fine-grained coatings on fractures in the ores. Schafarzikite was observed to be both older and younger than kermesite. At Pernek-Křížnica, crystals of kermesite or valentinite are sometimes overgrown by euhedral senarmontite (Fig. 4d). All of these minerals were formed by late hydrothermal remobilization and not by weathering of the ores.

Chemical composition of the Sb minerals

The major, minor, and trace element concentrations in all investigated minerals analyzed by EMP and LA-ICP-MS are shown in Table S1. Where applicable in this section, mean values are given together with two standard deviations of the measurements. Stibnite-II conforms to the stoichiometric formula Sb_2S_3 but its trace element concentrations are highly variable (Fig. 5). Arsenic content (measured with EMP) varies between 0.08 and 0.25 wt.%. The Zn concentrations range from 1.9 to 6.7 $\mu\text{g g}^{-1}$ (LA-ICP-MS), and those of Fe

Fig. 3 **a** A lens of massive stibnite, rimmed by gudmundite, parallel with the schistosity of the chlorite-actinolite schists. Pezinok-Trojárová. **b** Massive stibnite with a lens of native antimony. Pezinok-Kolársky vrch. **c** Intergrowth of native antimony, gudmundite, with later stibnite and latest valentinite. Note the relics of stibnite in valentinite (marked by the short white arrow). Reflected light, one nicol. Pezinok-Kolársky vrch

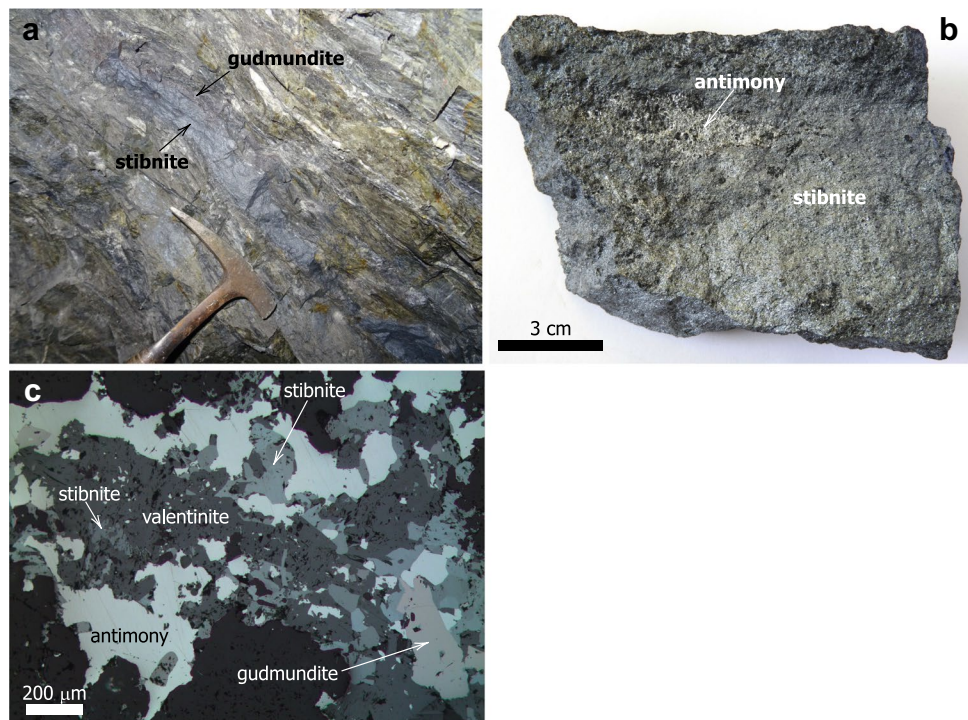
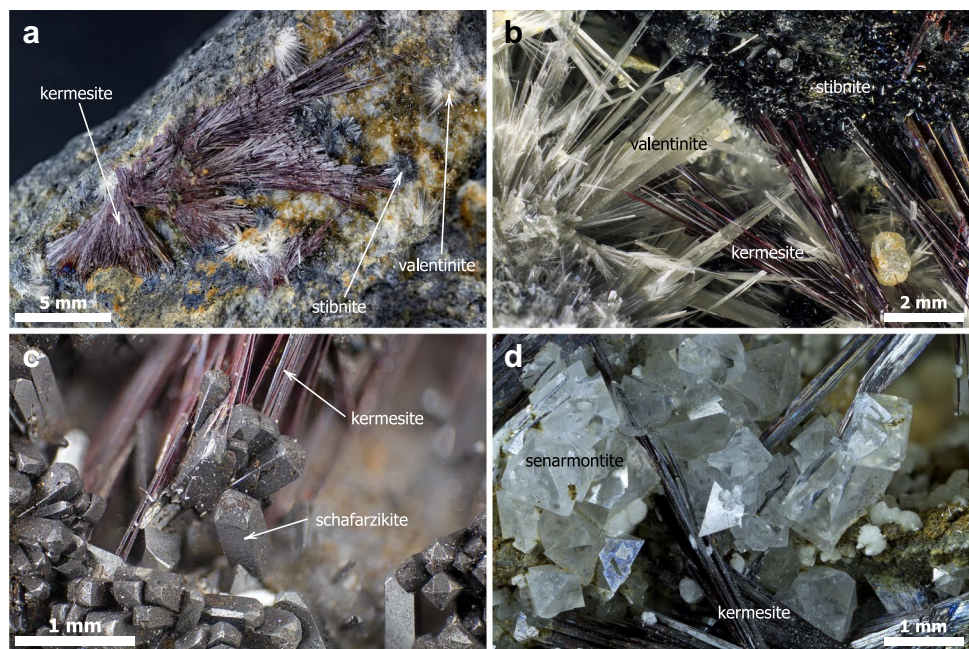


Fig. 4 Photographs of the mineralization in fractures from Pezinok-Trojárová (**a, b**) and Pernek (**c, d**). **a** Radial aggregates of stibnite are overgrown by acicular kermesite and acicular valentinite. **b** Fine needles of stibnite are overgrown by kermesite and valentinite. **c** A druse of schafarzikite crystals with kermesite needles. **d** Kermesite needles with octahedral senarmonite crystals



from $24.1 \mu\text{g g}^{-1}$ to 2.3 wt.% (measured with LA-ICP-MS and EMP, respectively). Silver was detected in stibnite with an average content of $0.4 \pm 1.3 \mu\text{g g}^{-1}$, whereas Au concentrations were below the detection limit of $0.06 \mu\text{g g}^{-1}$ (both measured with LA-ICP-MS).

Gudmundite has an average formula $\text{Fe}_{0.98}\text{Sb}_{1.05}\text{S}_{0.96}$, with an average Sb/(Sb + As) (molar ratio) of 0.995. Besides the

major elements, gudmundite contains up to 0.7 wt.% As (EMP) and an average Au content of $0.4 \pm 0.8 \mu\text{g g}^{-1}$ (LA-ICP-MS), while Zn is below the detection limit of $2.2 \mu\text{g g}^{-1}$.

Berthierite is close to the nominal composition FeSb_2S_4 and marked by slightly elevated As and Zn contents of up to 0.28 wt.% and $62.9 \mu\text{g g}^{-1}$, respectively (Fig. 5). In comparison to stibnite, berthierite shows elevated Ag concentration

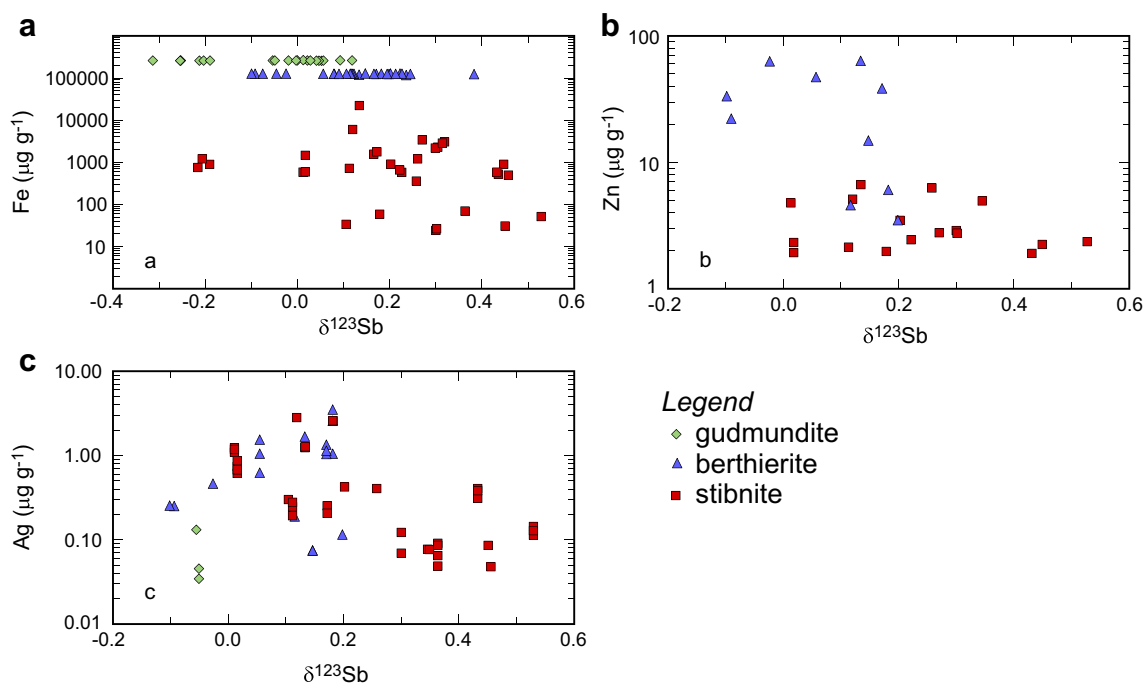


Fig. 5 $\delta^{123}\text{Sb}$ values versus **a** Fe, **b** Zn, and **c** Ag concentration in gudmundite (green diamonds), berthierite (blue triangles), and stibnite (red squares). Note the logarithmic ordinate of **a**, **b**, and **c**. Error bars are smaller than the symbol size

($0.88 \pm 1.75 \mu\text{g g}^{-1}$), whereas Au ($0.13 \mu\text{g g}^{-1}$) could be detected only in a single spot.

EMP analyses of native Sb and valentinite-senarmontite show that these minerals are composed of almost pure Sb ($99.7 \pm 0.2 \text{ wt.}\%$) or Sb_2O_3 ($99.7 \pm 0.3 \text{ wt.}\%$), respectively. In all three minerals, only minor impurities of As ($0.1\text{--}0.3 \text{ wt.}\%$) were detected (Table S1).

Kermesite is close to the nominal formula $\text{Sb}_2\text{S}_2\text{O}$. Schafarzikite from Pernek contains $82.1 \pm 0.3 \text{ wt.}\%$ Sb_2O_3 , $17.6 \pm 0.3 \text{ wt.}\%$ FeO, and minor As_2O_3 ($0.18 \pm 0.07 \text{ wt.}\%$) contents which correspond to the average formula $\text{Fe}_{0.96}(\text{Sb}_{2.03}\text{As}_{0.01})\text{O}_4$. Neither kermesite nor schafarzikite was analyzed for their trace elements with LA-ICP-MS.

Antimony isotopic composition

In order to distinguish the intra-mineral, inter-mineral, and inter-deposit heterogeneities, this work focused on polished sections with multiple Sb minerals with identifiable precipitation sequence. The $\delta^{123}\text{Sb}$ values of the primary Sb minerals (Fig. 6, Table S1) vary by almost 1.3‰ , from -0.4 and $+0.8\text{‰}$. Significant isotopic heterogeneity was found in some cases in a single mineral aggregate within one sample. For example, $\delta^{123}\text{Sb}$ values in stibnite from the sample PK3

vary between -0.19 and $+0.46\text{‰}$ at micrometer scales (Fig. 6). In addition to the local heterogeneities, individual minerals, for example, stibnite, show a range of $\delta^{123}\text{Sb}$ values of almost $+0.8\text{‰}$ in different samples and in different deposits studied in this work (Fig. 6).

Within a single sample composed of several minerals, the ranges of $\delta^{123}\text{Sb}$ values observed for each type of mineral overlap; however, their mean values are significantly different at 95% uncertainty levels and become progressively higher for younger minerals. In order to provide a measure for the uncertainty of the mean value for each mineral, we here provide the 2 standard error of the mean (2 SE) for each mineral. For the isotopic variability (2 SD) of individual minerals, the reader is referred to Figure 6. Within substage II, gudmundite shows in all sections the lowest Sb isotope values (median: $\delta^{123}\text{Sb} = -0.01 \pm 0.06\text{‰}$ (2 SE, $n = 22$)) compared to the berthierite ($+0.15 \pm 0.04\text{‰}$ (2 SE, $n = 31$)), stibnite ($+0.31 \pm 0.04\text{‰}$ (2 SE, $n = 63$)), and valentinite ($+0.46 \pm 0.09\text{‰}$, (2 SE, $n = 15$)) (Fig. 6; Table S1). A minor exception is the section PT2 where gudmundite has the lowest values ($-0.05 \pm 0.07\text{‰}$ (2 SE, $n = 4$)) but the isotopic compositions of berthierite ($+0.15 \pm 0.05\text{‰}$ (2 SE, $n = 1$)) and stibnite ($+0.18 \pm 0.04\text{‰}$ (2 SE, $n = 4$)) are identical within analytical uncertainties. In

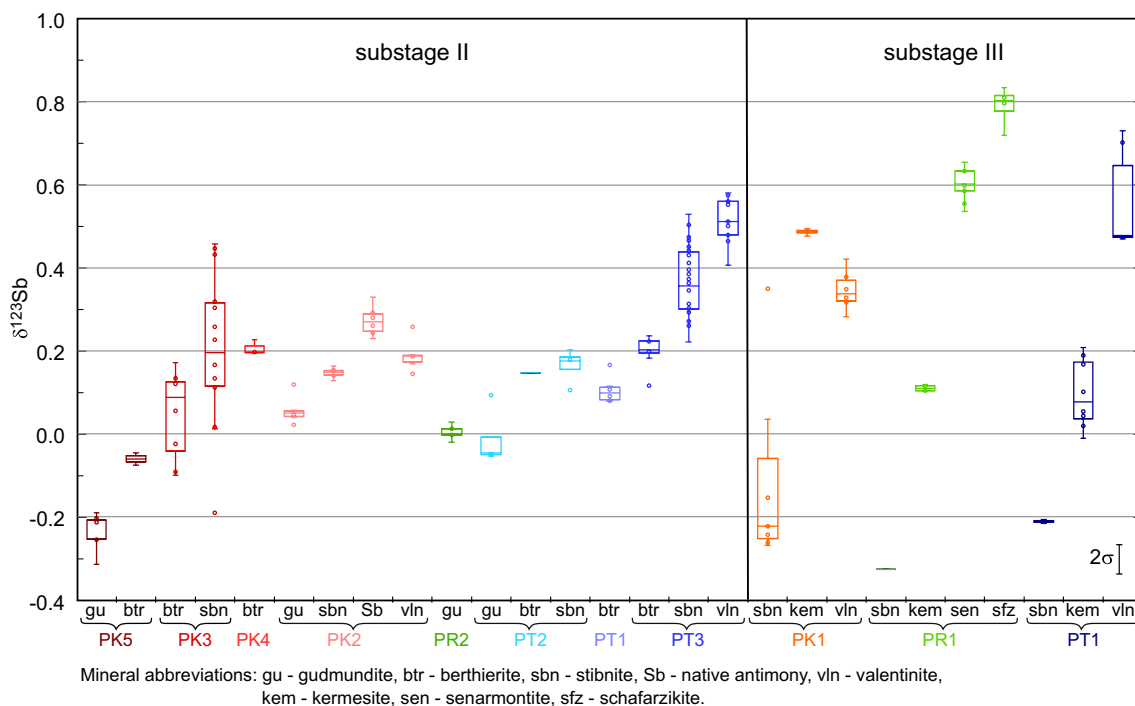


Fig. 6 Box plot showing all $\delta^{123}\text{Sb}$ values of the studied primary Sb minerals determined by fs-LA-MC-ICP-MS (Table S1). The individual polished sections in which the values were measured are color coded. The minerals were arranged according to their precipitation sequence. All $\delta^{123}\text{Sb}$ values are reported relative to NIST SRM 3102a (Kaufmann et al. 2021) standard. The whiskers and the box represent

the 5th, 25th, 75th, and 95th percentiles; the horizontal line within the box is the median. Representative 2σ error bars are given in the lower right corner, corresponding to the average error-propagated internal uncertainties (2 SE) of the sample and standard measurements (calculated as described by Horn et al. 2006)

contrast, the section PT3 showed significant isotopic differences between berthierite ($+0.20 \pm 0.03\text{‰}$ (2 SE, $n = 8$) and stibnite ($+0.37 \pm 0.03\text{‰}$ (2 SE, $n = 39$), with preferential enrichment of the heavy Sb isotope in stibnite. Valentinite in substage II displays two different patterns. In section PK2, valentinite is marked by an average slightly heavier $\delta^{123}\text{Sb}$ value ($+0.19 \pm 0.03\text{‰}$ (2 SE, $n = 6$) vs. $+0.15 \pm 0.01\text{‰}$ (2 SE, $n = 6$) compared to the coexistent stibnite. Conversely, section PT3 shows local signs of replacement of Sb sulfides (mostly stibnite) by Sb oxides. In such cases, the Sb isotopic signature of the Sb oxide shows an isotopic shift of $+0.10$ to $+0.31\text{‰}$ compared to that of the Sb sulfide.

The $\delta^{123}\text{Sb}$ values for the stibnite-III (Fig. 6) are $-0.22 \pm 0.13\text{‰}$ (2 SE, $n = 10$), much lower than those in stibnite-II. They are comparable or even lower than those for gudmundite-II. Within substage III, kermesite ($+0.12 \pm 0.09\text{‰}$ (2 SE, $n = 16$), valentinite ($+0.42 \pm 0.075\text{‰}$ (2 SE, $n = 11$)), and senarmontite ($+0.60 \pm 0.03\text{‰}$ (2 SE, $n = 9$)) record a distinct increase of the $\delta^{123}\text{Sb}$ values (Fig. 6) that can be correlated to the position of these minerals in the precipitation sequence. The analyzed schafarikite crystals (sample PR1) are marked by the highest $\delta^{123}\text{Sb}$ ($+0.80 \pm 0.05\text{‰}$ (2 SE, $n = 4$)).

Discussion

Antimony isotope fractionation processes

Antimony is transported mainly in hydrothermal fluids as Sb(III), in low- to moderately saline fluids as $\text{Sb}(\text{OH})_3^0$ or $\text{H}_2\text{Sb}_2\text{S}_4^0$ (Tossell 1994; Zotov et al. 2003; Bessinger and Apps 2005; Pokrovski et al. 2006; Olsen et al. 2018, 2019). In contrast, the presence of Sb(V) species in a hydrothermal fluid was reported only in alkaline fluids under oxidizing conditions (Zotov et al. 2003). Fluid inclusion analyses and thermodynamic estimates of oxygen fugacities of substages II and III (Bukovina 2006; Majzlan et al. 2020a) exclude the possibility of the transport of Sb as Sb(V) in alkaline fluids under oxidizing conditions. Therefore, it is likely that no redox change of Sb occurred during the precipitation of stibnite, berthierite, kermesite, senarmontite, or valentinite. In contrast, during the formation of gudmundite, Sb(III) in the fluid must be reduced to Sb(-I) in the solid. Precipitation of native antimony requires a reduction of Sb(III) to Sb(0). In general, reduction is expected to result in the enrichment of the lighter isotopes in the product (e.g., Rouxel et al. 2003; Markl et al. 2006; MacKinney 2016), because of the generally weaker bonding of the reduced species.

For antimony, the reduction from Sb(V) to Sb(III) is known to be associated with large fractionation factors of -0.9 to -1.4‰ at room temperature (Rouxel et al. 2003; MacKinney 2016). To our best knowledge, no data exist for

the isotopic fractionation during the reduction of Sb(III) to Sb(0) or Sb(-I). The fractionation factors for the Sb(V)-Sb(III) reduction may be taken as a rough proxy for those expected for the Sb(III)-Sb(-I) reduction and corrected for temperature, as proposed by Welch et al. (2003) or Ehrlich et al. (2004). With such an approach, the observed fractionation of -1.2‰ at 20 °C (Rouxel et al. 2003; MacKinney 2016) would correspond to fractionation of -0.3‰ at $\sim 300\text{ °C}$ (calculated as $-1.2 \times (20 + 273)^2 / (300 + 273)^2$).

In a recent work, Zhai et al. (2021) roughly estimated the fractionation factor between stibnite and fluid (both containing Sb(III)) as $\alpha_{\text{fluid-stibnite}} = 0.9994$ at around 200 °C (Hu and Peng 2018). This factor translates to an isotopic difference between the fluid and stibnite of $\Delta^{123}\text{Sb}_{\text{fluid-stibnite}} = 1000 \ln \alpha_{\text{fluid-stibnite}} = -0.6$, meaning that stibnite that precipitates from a hydrothermal fluid should be isotopically lighter than the fluid. Hence, the sparse data imply that the precipitation of hydrothermal Sb minerals is expected to deplete the fluid in the lighter isotope ^{121}Sb , independently from the redox reactions of Sb.

Furthermore, as shown for other metals (e.g., Cu, Graham et al. 2004; Gregory and Mathur 2017), the successive deposition of isotopically heavier minerals may also be related to a partial depletion of the metal source, if light metal isotopes are preferentially mobilized. In this scenario, the source material would become isotopically heavier with time and will produce successively isotopically heavier mineral depositions.

Formation of the mineralization in substage II

Textural, trace element, and Sb isotopic trends in substage II

The main Sb mineral in the studied ore deposits is stibnite. There is, however, no textural evidence of multiple stibnite-II generations. Yet, a larger variation (from $\sim 0.1\text{‰}$ up to $\sim 0.5\text{‰}$) in $\delta^{123}\text{Sb}$ values within the stibnite-II masses is observed. A correlation between several trace elements, such as Fe, Zn, or Ag (Fig. 5), and the $\delta^{123}\text{Sb}$ values indicate prolonged precipitation of stibnite. This precipitation was accompanied by isotopic fractionation (shift to higher $\delta^{123}\text{Sb}$ values in stibnite) and chemical modifications, i.e., uptake of the trace elements into stibnite and their depletion in the fluid. Some of these elements can be taken up into the structure of the crystallizing stibnite (e.g., arsenic, Fu et al. 2020), others (Zn, Fe) could form nanoinclusions in the stibnite matrix.

A systematic trend of increasing $\delta^{123}\text{Sb}$ values during the progress of ore formation is discernible in all studied sections (Fig. 6) on millimeter to micrometer scale. It is compatible with the depletion of the hydrothermal fluid in heavier Sb isotopes. An increase in the $\delta^{123}\text{Sb}$ values by

successively crystallized stibnite has already been observed by Zhai et al. (2021). Thus, a similar scenario as for stibnite likely applies in general for the successive crystallization of all antimony minerals during the substage II. Gudmundite formed as one of the first minerals in the substage II in the studied ore deposits. It is followed by crystallization of berthierite and later stibnite, the latter displaying diminishing trace element contents and increasing $\delta^{123}\text{Sb}$ values (Fig. 5 and Fig. 6). The Sb sulfide sequence is followed by crystallization of the late valentinite-II that is isotopically heavier than the Sb sulfides of substage II (Fig. 6).

In some cases, the $\delta^{123}\text{Sb}$ values are indistinguishable for spatially associated berthierite-II and stibnite-II. This similarity in the $\delta^{123}\text{Sb}$ values may imply simultaneous precipitation of the two minerals, assuming their mineral-fluid fractionation factors are similar. Alternatively, or parallel to the previous explanation, gudmundite-II replacement by stibnite, as indicated by textural evidence, can also lead to inherited lower $\delta^{123}\text{Sb}$ value in stibnite-II.

The only exception to the steady increase of $\delta^{123}\text{Sb}$ value along the precipitation sequence was observed in section PK2. Here, the late valentinite-II has a $\delta^{123}\text{Sb}$ value of +0.19‰, similar to the coexisting stibnite-II (+0.15‰) but lower than that observed for native antimony (+0.27‰). In this case, valentinite-II replaces stibnite-II and probably inherited almost totally its isotopic composition from stibnite-II.

Physicochemical conditions and duration of ore deposit formation

Temperature decrease is considered the main precipitation mechanism of stibnite (Williams-Jones and Normand 1997). Large data sets show that the mean Sb concentrations in natural hydrothermal fluids are 10.7 ppm (Naumov et al. 2018), with a large range within the 95% envelope from 1.8 to 64.8 ppm. There is no information if these concentrations refer to fluids before or after Sb mineral precipitation but the order of magnitude of solubilities conforms to the predictions from thermodynamic data (Williams-Jones and Normand 1997) regarding solubility of stibnite. The start of precipitation of stibnite at ~ 200 °C would require starting Sb concentrations of a few ppm Sb (Williams-Jones and Normand 1997), at the lower end of the range reported by Naumov et al. (2018). The strong temperature dependence of Sb solubility means the Sb precipitated from a fluid will not be re-dissolved as long as the fluid remains reducing. This is in line with the steady increase of the $\delta^{123}\text{Sb}$ values along the precipitation sequence and can be described by a simple Rayleigh model (Fig. 7):

$$\delta^{123}\text{Sb}_{\text{fluid}} = (\delta^{123}\text{Sb}_{\text{fluid}_t0} + 1000)F^{(\alpha-1)} - 1000$$

where $\delta^{123}\text{Sb}_{\text{fluid}}$ represents the isotope ratio of the hydrothermal fluid; $\delta^{123}\text{Sb}_{\text{fluid}_t0}$ is the initial isotope composition of the hydrothermal fluid; and F is the fraction of the residual Sb in solution and fractionation factor α is given by $R_{\text{fluid}}/R_{\text{precipitate}}$. For a simple evaluation of this model, we apply the α value proposed by Zhai et al. (2021) of 0.9994. In the absence of other data, this fractionation factor is applied to all minerals observed in the substage II. We assume that the initial $\delta^{123}\text{Sb}_{\text{fluid}_t0}$ was +0.3‰, a value that corresponds to the mean Sb isotopic composition of the abundant stibnite-II. In that model, the first precipitate will have $\delta^{123}\text{Sb}$ value of -0.3‰, whereas at larger values of F , the resulting precipitate may be isotopically heavier than the initial fluid. In such a scenario, assuming continuous precipitation and no backward dissolution, precipitation of 60–70% of the Sb in the fluid is required to produce the observed isotopic range in substage II (Fig. 6, 7a).

Precipitation sequence in substage II

The samples used in this work were selected to capture different stages of the evolution of the studied ore deposits. The precipitation sequence and the relative timing of the minerals was investigated by Cambel (1959), Andr  s (1983), Chovan et al. (1994), Bukovina (2006), and Chovan et al. (2006). All these authors agree that the hydrothermal precipitation commenced with quartz and Au-bearing pyrite and arsenopyrite with minor gudmundite in substage I. These minerals were followed by precipitation of quartz-carbonate-stibnite with less abundant native antimony, gudmundite, pyrrhotite, and berthierite in substage II.

Andr  s (1983) and Chovan et al. (1994) interpreted gudmundite and berthierite (consistent with the presence of Au determined by LA-ICP-MS) as being older than native antimony. In contrast, Bukovina (2006) suggested that microscopic observations alone may be insufficient to determine the paragenetic position of native antimony and used the phase diagrams of Williams-Jones and Normand (1997) to postulate that native antimony is one of the oldest Sb minerals.

Following the reasoning from above, we may use the Sb isotopic composition as a tool to better constrain the precipitation sequence. Namely, the trends of isotopic composition appear to be closely correlated with the position of the minerals in the precipitation sequence (Figs. 6 and 7). The early minerals (gudmundite and berthierite) are always isotopically lighter with higher trace element content. During progressive precipitation, the later Sb minerals (stibnite-II and valentinite-II) become successively isotopically heavier (median values (± 2 SE) $\delta^{123}\text{Sb}_{\text{gu}} = -0.01 \pm 0.06\text{‰}$, $\delta^{123}\text{Sb}_{\text{btr}} = +0.15 \pm 0.04\text{‰}$, $\delta^{123}\text{Sb}_{\text{sbn}} = +0.31 \pm$

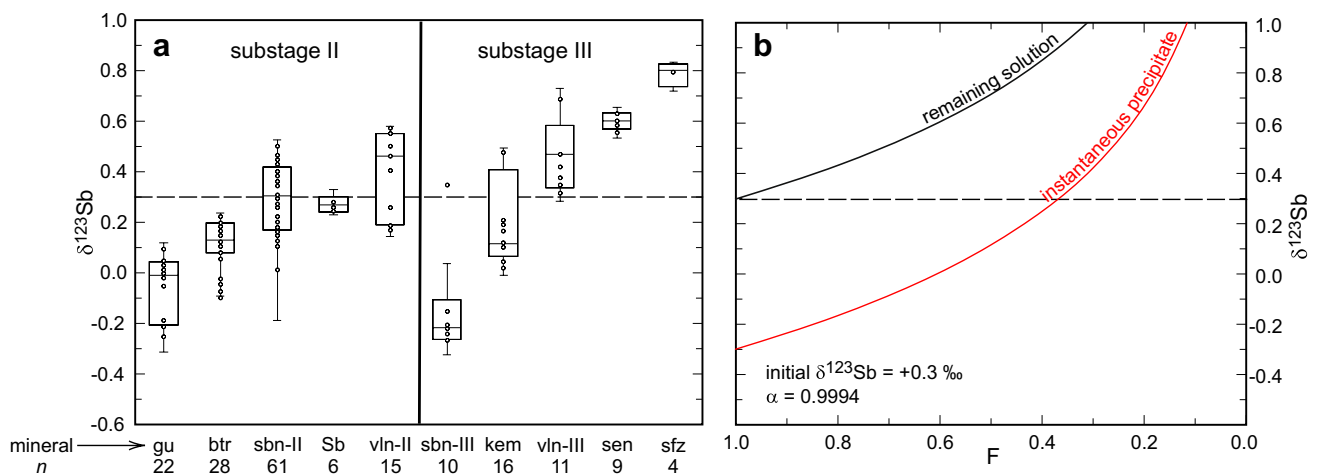


Fig. 7 **a** A summary of the isotopic composition of the minerals in the Sb-As-Au mineralization, illustrated as box plots. **b** A Rayleigh model calculation showing the isotope composition of a precipitate and remaining fluid. The red curve represents an example for instantaneous precipitation ($\alpha = 0.9994$, Zhai et al. 2021) forming from a

hydrothermal fluid with an initial $\delta^{123}\text{Sb}$ of + 0.3‰. In this model, the precipitate would form from residual fluids enriched in heavy Sb during previous precipitation events. The mineral abbreviations are the same as in Fig. 6

0.04‰, $\delta^{123}\text{Sb}_{\text{vl-II}} = +0.46 \pm 0.09\%$, Fig. 7). The isotopic changes can be quantitatively interpreted with a simple Rayleigh model. Assuming that the model applies to all minerals, using a single mineral-fluid fractionation factor, native antimony appears to be one of the later, not the first mineral in substage II (Fig. 8). Textural evidence observed in our samples supports the implications derived from Sb isotopic signatures. Native antimony is found as aggregates within the Sb sulfides, mostly stibnite (Fig. 3b). We interpret this texture as precipitation of stibnite up to the exhaustion of sulfur supply in the fluid and subsequent precipitation of native antimony. In this case, native antimony is coeval or younger than stibnite or other Sb sulfides, just as shown in Figs. 6 and 8. An additional new finding is the formation of Sb oxide, valentinite, at the end of the substage II (Fig. 3c) simultaneously or after the stibnite formation. This valentinite-II, probably formed upon the exhaustion of sulfide in the system, has similar or heavier $\delta^{123}\text{Sb}$ values than the neighboring stibnite (median: $\delta^{123}\text{Sb}_{\text{sbn}} = +0.31 \pm 0.04\%$, $\delta^{123}\text{Sb}_{\text{vl-II}} = +0.46 \pm 0.09\%$ (2 SE)). Thus, using antimony isotopes, we were able to resolve the questions related to the precipitation sequence which were difficult to tackle by textural studies in the past (Andráš 1983; Chovan et al. 1994, 2006; Bukovina 2006).

Formation of the mineralization in the substage III

The mineralization of substage III is located in thin fractures and is clearly texturally later than the substages I and II. Aggregates of euhedral stibnite-III, kermesite, valentinite-III, senarmontite, and schafarzikite (Fig. 4) are volumetrically minor, but represent a conspicuous and unique

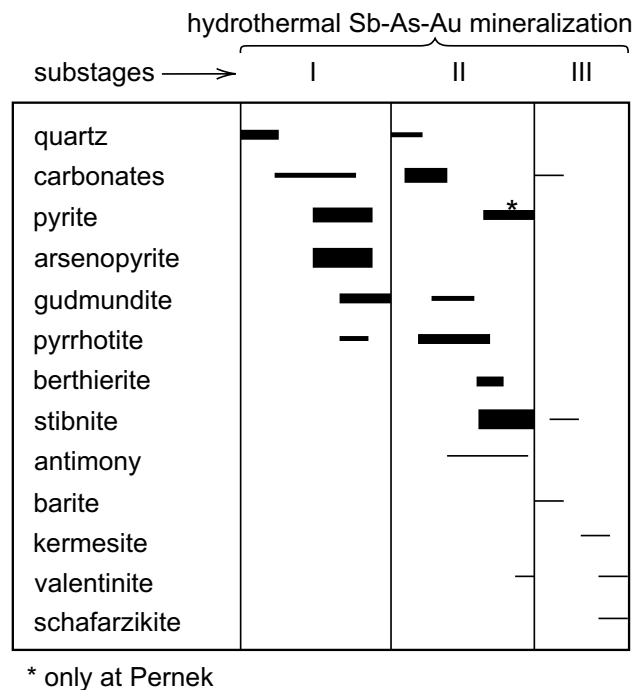


Fig. 8 Precipitation sequence of the hydrothermal Sb-As-Au mineralization in the deposits studied, after Bukovina (2006) and Chovan et al. (2006), with modifications explained in the text. The individual substages, delineated in the diagram by vertical lines, are separated by intermineralization tectonics

component of the ore bodies at Pezinok and Pernek. Schafarzikite occurs only at Pernek, presumably because the primary ores are composed of abundant stibnite and pyrite that were able to supply Sb and Fe simultaneously in the

remobilizing fluids. Similar to substage II, the precipitation sequence of substage III, from the older to the younger minerals, is also well correlated to the $\delta^{123}\text{Sb}$ values of the minerals (Fig. 3, Fig. 7). The $\delta^{123}\text{Sb}$ values between the substages II and III are not continuously linked, however. There is a distinct offset between the latest minerals of the substage II and stibnite-III (Fig. 7a).

The substage III is restricted to fractures that crosscut the ores of the substage II and constitutes a late hydrothermal overprint of the main mineralization. As already mentioned earlier in this publication, these minerals are by no means related to weathering. Fluid inclusion and traditional stable isotopes ($\delta^{18}\text{O}$, $\delta^{13}\text{C}$, $\delta^{34}\text{S}$; Chovan et al. 1992; Andr  s et al. 2003; Majzlan et al. 2020a and references therein) suggest that one of the main components of the fluids in substage III was water of meteoric or marine origin. Such fluids, however, are unlikely to bring a significant Sb input into the deposit. Thus, we suggest that these fluids may have leached and remobilized small volumes of the substage II mineralization. Primary, hydrothermal kermesite and valentinite are uncommon but when they occur, they are considered to be reworking of earlier sulfide mineralization by younger oxidizing fluids (Normand et al. 1996).

An origin of substage III Sb from remobilization of substage II Sb is furthermore supported by the very similar initial Sb isotopic composition of the substages II and III, indicating that the fluids in substage III likely inherited their Sb isotopic signature from stibnite-II. In such a scenario, the $\delta^{123}\text{Sb}$ values determined for stibnite-III (Fig. 7) can be well explained by mineral-fluid fractionation with the $\alpha_{\text{fluid-stibnite}} = 0.9994$ (Zhai et al. 2021) and we can model the trend of continuously increasing $\delta^{123}\text{Sb}$ values observed for substage III minerals to be the result of progressive mineral precipitation (Fig. 6) applying a Rayleigh fractionation model, similar to that suggested for substage II mineralization (Fig. 7). The larger range towards heavier $\delta^{123}\text{Sb}$ values observed for substage III compared to that of substage II (Fig. 7a) may be explained by a higher exhaustion of Sb in the fluid during progressive Sb mineral precipitation which may indicate a higher initial Sb concentration, likely because of the higher Sb solubility in oxidizing or sulfur-poor fluids (Williams-Jones and Normand 1997).

Models of Sb ore deposit formation

Our data offer some qualitative implications regarding the nature of the precipitation process and its duration. The notion of rapid precipitation within hours or days is inconsistent with isotopic heterogeneities of around 0.6‰ at the mm to km scale in the minerals studied. Our data show convincingly an isotopic shift towards higher $\delta^{123}\text{Sb}$ values as the precipitation proceeds. This isotopic trend is accompanied by trace element depletion in later precipitated minerals

(Fig. 5; e.g., Ag content in stibnite decreases from ~ 2.9 to $< 0.1 \mu\text{g g}^{-1}$ as the precipitation proceeds). Such isotopic and trace element variations could arise from (i) a continuous change in the metal source generated during progressive metal mobilization by a fluid; (ii) slow precipitation from a single fluid batch that mobilized metal from a homogenous metal source and that became depleted in trace metals and light Sb isotopes during progressive mineral precipitation; or (iii) episodic metal precipitation from multiple fluid batches that mobilized metals from the same source(s) and that became depleted in trace metals and light Sb isotopes during progressive mineral precipitation.

The first option (i) fractionation of Sb isotopes in the source during Sb mobilization cannot be excluded; however, it is considered to be unlikely significant. At high temperatures of $\sim 850\text{--}1000 \text{ }^\circ\text{C}$, a recent experimental study by Fu et al. (2020) indicated that Sb only weakly partitions into aqueous chloride-bearing fluids in rhyolitic systems, and isotope fractionation at such high temperatures is expected to be low. At lower temperatures of 400 to 300 $^\circ\text{C}$, i.e., under hydrothermal-metamorphic conditions, experimental studies and natural fluid inclusion data (Aud  t et al. 2000; Zajacz et al. 2008; Naumov et al. 2018) indicate high antimony content in the fluid phase present as $\text{Sb}(\text{OH})_3^0$ (Pokrovski et al. 2005, 2006). In this case, however, Sb is almost quantitatively removed from the source without isotopic fractionation. Such a scenario applies also to the prograde metamorphism where Sb is released during the breakdown of pyrite or rutile (at $T = 250\text{--}450 \text{ }^\circ\text{C}$; Pitcairn et al. 2006, 2015). Thus, the fractionation in the source alone is unlikely to generate the 0.6‰ $\delta^{123}\text{Sb}$ variations observed in the ore deposits studied in this work.

Precipitation from a single fluid pulse (ii) may produce the observed shift in $\delta^{123}\text{Sb}$ values; however, considering the solubility of Sb (e.g., Williams-Jones and Normand 1997; Zotov et al. 2003), an unrealistically large volume of fluid would be required. Assuming that stibnite started precipitating at 180 $^\circ\text{C}$ (as shown by the fluid inclusion data), the fluid would be saturated with respect to stibnite at 8 ppm Sb and assumed 0.01 M H_2S under reducing conditions (Williams-Jones and Normand 1997). In such a case, 100–700 m^3 of fluid would be required to precipitate 1 kg of stibnite. Accordingly, the fluid must have been episodically replenished over geological time scales, leading to option (iii).

A scenario of successive pulses of ore-forming fluid, penetrating into the metamorphosed black shales, holds certainly for the three distinct substages, including the lenses formed in substage I, followed by the stibnite-rich lenses in substage II, and the mineralization in fractures of the substage III. An additional argument that supports the notion of several fluid pulses for the formation of Sb mineralization at Pezinko is the different mean $\delta^{123}\text{Sb}$ values of the substage II minerals in the studied ore deposits. The mean $\delta^{123}\text{Sb}$ values

for all measured minerals and stibnite at Kolársky vrch are $+0.10\%$ ($n = 59$) and $+0.18\%$ ($n = 21$), respectively. At Trojárová, they are $+0.31\%$ ($n = 68$) and $+0.35\%$ ($n = 40$), respectively. Although the Sb isotopic ranges observed for the two deposits overlap, Kolársky vrch has a mean $\delta^{123}\text{Sb}$ value that is lower than that of the Trojárová ore body and, therefore, probably younger in age. Thus, ore-forming fluids likely developed progressively and differently during ore formation. This is also supported by the thin, submillimeter coatings of stibnite in the surrounding schists or gneisses which points out at early or first precipitates that have isotopically fractionated the remaining fluids towards heavier values. Thus far, only scarce Sb isotope data of hydrothermal Sb deposits exist that could be compared to our data. However, the mean $\delta^{123}\text{Sb}$ value of $\sim +0.3\%$ of the most abundant mineral stibnite can explain the entire isotopic range observed in Fig. 7 and indicates that ore formation overall results in little Sb isotope fractionation relative to the continental crust (Wen et al. 2018 and ref. therein).

The timing of the tectonic development may provide additional information about the episodic origin of the studied mineralizations. The studied deposits are considered to be of late-Variscan (~ 320 Ma) age, in analogy with similar stibnite deposits in the Tatric Superunit (Majzlan et al. 2020b). In this time, the Variscan igneous and metamorphic complexes experienced rapid exhumation and cooling, with cooling rates of $20\text{--}40$ °C/Ma (Moussallam et al. 2012). Such cooling rates are comparable to those determined for other Variscan complexes in Europe, such as the Black Forest (Weyer et al. 1999) or the Brittany Massif (Brown and Dallmeyer 1996) but they may apply to higher-temperature conditions (> 200 °C) of the retrograde metamorphism. With an assumed cooling rate of 10 °C/Ma for the cooling below 200 °C, it would have taken ~ 6 Ma to cool the host rocks from the beginning to the end of stibnite precipitation ($180\text{--}120$ °C, Bukovina 2006). Such time interval is comparable to the order of magnitude needed for subduction and associated volcanism (Hu and Gurnis 2020), assembly of igneous plutons (Ducea et al. 2015), or operation of regional fluid systems (Beinlich et al. 2020).

There is mounting evidence that events related to fluid motion and mineral precipitation in such systems are episodic and fast, even though repeated over longer geological time spans. Such episodes, called flare-ups for igneous systems, can dwarf longer but quiescent time periods in terms of their productivity. Fluid release from rocks during prograde metamorphism is also considered to be episodic, with episodes on time scales of $10^3\text{--}10^5$ years (van Haren et al. 1996; Graham et al. 1998; Connolly 1997, 2010). Fluid release from subducting slabs occurs in pulses with a duration of ~ 200 years and such pulses are episodically repeated over millions of years (John et al. 2012). Orogenic deposits seem to form as an aftermath of repeated seismic events and

episodic fluid pulses (Goldfarb and Pitcairn 2023). Thus, independent from the ore source, magmatic, or orogenic, several fluid pulses for the formation of these Sb ore deposits are needed.

Implications and conclusions

The Sb isotopic and trace-element data collected in this work document the applicability of Sb isotopes in the study of ore-forming processes and provide unique insights into the formation of ore deposits. A remarkable feature is the systematic isotopic shift towards higher $\delta^{123}\text{Sb}$ values during progressive precipitation of Sb minerals. That means that the sequence of Sb ore formation is recorded by the isotopic signature of Sb minerals. A similar relationship was previously postulated for stibnite mineralization (Zhai et al. 2021). Here, we demonstrated that a similar trend can be recorded in diverse Sb minerals, not only in stibnite. This trend is discernible in both substages II and III, even though they feature different assemblages, from phases with Sb(-I) to Sb(III) sulfoxides and oxides.

A notable limitation of the model presented in this work and the use of antimony isotopes in hydrothermal systems is the lack of mineral-fluid fractionation factors. There is only one estimate available for stibnite (Zhai et al. 2021). Even though this estimate appears to be reasonable in light of our data, more work must be invested in the determination of Sb isotope fractionation factors in order to make Sb isotopes a suitable tool to accurately reconstruct the formation and operation of hydrothermal ore-forming systems.

Variations of the $\delta^{123}\text{Sb}$ values within a single, small to medium-sized deposit camps (i.e., the studied deposits near Pezinok and Pernek) could make the tracking of the source of Sb in such deposit problematic. The investigations of the Sb isotope system, however, are in the beginning when compared to other metal-isotope systems and possible sources of Sb are at present poorly constrained. It seems that the Sb isotopic composition of stibnite and other Sb minerals is a promising tool for understanding the fluid origin of the metalloid, although more work needs to be done to be able to link different sources and their ores.

Despite the limitations of our model, our findings may help to constrain precipitation sequences in ore deposits, decipher hydrothermal remobilization or weathering episodes of the ores, or deduce which parts of the hydrothermal systems are being exploited. Taking into account that the heavier isotopic compositions appear to be related to late mineralization stages, it could be worthwhile to search for earlier, perhaps more voluminous Sb mineralization with a lighter $\delta^{123}\text{Sb}$ signature. Being often associated with deposits of Au or Ag (e.g., Ashley et al. 2000; Nevolko et al. 2018; Burisch et al. 2019; Qiu et al. 2020; Goldfarb and Pitcairn

2023), investigation of Sb minerals and their isotopic composition may also be useful for understanding and exploration of such ore deposits.

Supplementary Information The online version contains supplementary material available at <https://doi.org/10.1007/s00126-023-01222-7>.

Acknowledgements We are thankful to Ingo Horn for his support and helpful advise during the LA-MC-ICP-MS measurements and to Julian Feige for standard preparation. We thank Degao Zhai (editor), Ryan Mathur, and one anonymous reviewer for their constructive comment that helped to improve the manuscript.

Author contribution A.K. contributed to the analyses of Sb isotopes and trace elements with femtosecond laser ablation coupled (MC)-ICP-MS, data processing, petrography of the ore minerals, discussion of data, and writing the manuscript. M.L. contributed to the project design, analytical support with fs-LA-(MC)-ICP-MS, data processing, interpretation + discussion of data, and writing of the manuscript. S.W. contributed to the interpretation + discussion of data and writing of the manuscript. M.S. contributed to sample selection + petrography of the samples and S.K. performed the EMPA measurements. J.M. contributed to the project design, sample selection, petrography, interpretation + discussion of the data, and writing of the manuscript.

Funding Open Access funding enabled and organized by Projekt DEAL. This study was financially supported by the *Deutsche Forschungsgemeinschaft* (grant LA 3392/3-1 and MA 3927/32-1) which is gratefully acknowledged. M.Š. is thankful for funding from the grant APVV-22-0041.

Declarations

Conflict of interest The authors declare no competing interests.

Open Access This article is licensed under a Creative Commons Attribution 4.0 International License, which permits use, sharing, adaptation, distribution and reproduction in any medium or format, as long as you give appropriate credit to the original author(s) and the source, provide a link to the Creative Commons licence, and indicate if changes were made. The images or other third party material in this article are included in the article's Creative Commons licence, unless indicated otherwise in a credit line to the material. If material is not included in the article's Creative Commons licence and your intended use is not permitted by statutory regulation or exceeds the permitted use, you will need to obtain permission directly from the copyright holder. To view a copy of this licence, visit <http://creativecommons.org/licenses/by/4.0/>.

References

- Andráš P (1983) Problems to the genesis of stibnite and gold mineralization at the deposit Pezinok. Dissertation. Geofond, Bratislava, p 159 in Slovak
- Andráš P, Chovan M (2001) Invisible gold in sulphides (Western Carpathians, Slovakia). In: Piestrzynski A (ed) Mineral deposits at the beginning of the 21st century. Swets & Zeitlinger B. V., Lisse, pp 511–514
- Andráš P, Luptáková J, Kotulová J (2003) Evolution of ore-forming fluids at Pezinok-Kolársky vrch Sb-Au deposit (Western Carpathians, Slovakia). Acta Mineral Petrogr. Abstract Series 1, Szeged
- Araki Y, Tanimizu M, Takahashi Y (2009) Antimony isotopic fractionation during adsorption on ferrihydrite. Geochim Cosmochim Acta Suppl 73:A49
- Ashley PM, Creagh CJ, Ryan CG (2000) Invisible gold in ore and mineral concentrates from the Hillgrove gold-antimony deposits, NSW, Australia. Miner Deposita 35(4):285–301. <https://doi.org/10.1007/s001260050242>
- Audétat A, Günther D, Heinrich CA (2000) Causes for large-scale metal zonation around mineralized plutons: fluid inclusion LA-ICP-MS evidence from the Mole Granite, Australia. Econ Geol 95(8):1563–1581. <https://doi.org/10.2113/gsecongeo.95.8.1563>
- Beinlich A, John T, Vrijmoed JC, Tominaga M, Magna T, Podladchikov YY (2020) Instantaneous rock transformations in the deep crust driven by reactive fluid flow. Nat Geosci 13:307–311. <https://doi.org/10.1038/s41561-020-0554-9>
- Bessinger B, Apps JA (2005) The hydrothermal chemistry of gold, arsenic, antimony, mercury and silver. Report LBNL-57395:52
- Brown M, Dallmeyer RD (1996) Rapid Variscan exhumation and the role of magma in core complex formation: southern Brittany metamorphic belt, France. J Metamorph Geol 14(3):361–379. <https://doi.org/10.1111/j.1525-1314.1996.00361.x>
- Bukovina J (2006) Hydrothermal Fe–Sb–S–O system: mineralogy and formation conditions (case study on the Sb deposits in the Malé Karpaty Mts.). Diploma Thesis. Comenius University, Bratislava, pp 1–49 (in Slovak)
- Burisch M, Hartmann A, Bach W, Krollop P, Krause J, Gutzmer J (2019) Genesis of hydrothermal silver-antimony-sulfide veins of the Bräunsdorf sector as part of the classic Freiberg silver mining district, Germany. Miner Depos 54:263–280. <https://doi.org/10.1007/s00126-018-0842-0>
- Cambel B (1959) Hydrothermal deposits in the Malé Karpaty Mts., mineralogy and geochemistry of their ores. Acta Geol Geogr Univ Com, Geol 3:1–234 (in Slovak)
- Cambel B, Mikláš J, Khun M, Veselský J (1990) Geochemistry and petrology of clay-metamorphic rocks of the Malé Karpaty Mts. Crystalline complex. Geol Inst Slovak Acad Sci, Bratislava, pp 1–267
- Chovan M, Háber M, Jeleň S, Rojkovič I (1994) Ore textures in the Western Carpathians. Slovak Academic Press, pp 1–219
- Chovan M, Hurai V, Putiš M, Ozdín D, Pršek J, Moravanský D, Luptáková J, Záhradníková J, Král J, Konečný P (2006) Fluid sources and formation of the mineralizations of the Tatric and northern Veporic units. In: Open File Report. Comenius University, Bratislava (in Slovak)
- Chovan M, Rojkovič I, Andráš P, Hanas P (1992) Ore mineralization of the Malé Karpaty Mts. (Western Carpathians). Geol Carpath 43:275–286
- Chovan M, Trtíková S, Viliňovič V, Khun M, Hanas P (2002) Ore mineralization on the Pezinok–Trojárová deposit in the Malé Karpaty Mts., Slovakia: mineralogical and geochemical characterization. Slov Geol Mag 8:179–193
- Connolly JAD (1997) Devolatilization-generated fluid pressure and deformation-propagated fluid flow during prograde regional metamorphism. J Geophys Res 102:18149–18173. <https://doi.org/10.1029/97JB00731>
- Connolly JAD (2010) The mechanics of metamorphic fluid expulsion. Element 6:165–172. <https://doi.org/10.2113/gselements.6.3.165>
- Degryse P, Shortland AJ, Dillis S, van Ham-Meert A, Vanhaecke F, Leeming P (2020) Isotopic evidence for the use of Caucasian antimony in Late Bronze Age glass making. J Archaeol Sci 120:105195. <https://doi.org/10.1016/j.jas.2020.105195>
- Dill H, Kus J, Dohrmann R, Tsou Y (2008) Supergene and hypogene alteration in the dual-use kaolin-bearing coal deposit Angren, SE

- Uzbekistan. *Int J Coal Geol* 75(4):225–240. <https://doi.org/10.1016/j.coal.2008.07.003>
- Ducea MN, Paterson SR, DeCelles PG (2015) High-volume magmatic events in subduction systems. *Elements* 11:99–104. <https://doi.org/10.2113/gselements.11.2.99>
- Ehrlich S, Butler I, Halicz RD, Oldroyd A, Matthews A (2004) Experimental study of the copper fractionation between aqueous (CuII) and coellite (CuS). *Chem Geol* 209:259–269. <https://doi.org/10.1016/j.chemgeo.2004.06.010>
- Fang Y, Chen K, Bao Z, Zong C, Yuan H, Lv N (2022) New analysis protocol for stable isotopes by a standard doping method – an example of antimony. *Anal Chem* 94:16746–16751. <https://doi.org/10.1021/acs.analchem.2c03420>
- Ferrari C, Méheut M, Resongles E, Freydier R, Casiot C (2022) Equilibrium mass-dependent isotope fractionation of antimony between stibnite and Sb secondary minerals: a first-principles study. *Chem Geol* 611:121115. <https://doi.org/10.1016/j.chemgeo.2022.121115>
- Ferrari C, Resongles E, Freydier R, Casiot C (2021) A single-step purification method for the precise determination of the antimony isotopic composition of environmental, geological and biological samples by HG-MC-ICP-MS. *J Anal At Spectrom* 36:776–785. <https://doi.org/10.1039/d0ja00452a>
- Fu S, Hu R, Bi X, Sullivan NA, Yan J (2020) Trace element composition of stibnite: substitution mechanism and implications for the genesis of Sb deposits in southern China. *Appl Geochemistry* 118:104637. <https://doi.org/10.1016/j.apgeochem.2020.104637>
- Gilbert S, Danyushevsky L, Robinson P, Wohlgemuth-Ueberwasser C, Pearson N, Savard D, Norman M, Hanley J (2013) A comparative study of five reference materials and lombard meteorite for the determination of the platinum-group elements and gold by LA-ICP-MS. *Geostand Geoanal Res* 37:51–64. <https://doi.org/10.1111/j.1751-908X.2012.00170.x>
- Goldfarb RJ, Pitcairn I (2023) Orogenic gold: is a genetic association with magmatism realistic? *Mineral Depos* 58:5–35. <https://doi.org/10.1007/s00126-022-01146-8>
- Graham CM, Valley JW, Eiler JM, Wada H (1998) Timescales and mechanisms of fluid infiltration in a marble: an ion microprobe study. *Contrib Mineral Petrol* 132:371–389
- Graham S, Pearson N, Jackson S, Griffin W, O'Reilly S (2004) Tracing Cu and Fe from source to porphyry: in situ determination of Cu and Fe isotope ratios in sulfides from the Grasberg Cu-Au deposit. *Chem Geol* 207:147–169. <https://doi.org/10.1016/j.chemgeo.2004.02.009>
- Gregory MJ, Mathur R (2017) Understanding copper isotope behavior in the high temperature magmatic-hydrothermal porphyry environment. *Geochim* 18:4000–4015. <https://doi.org/10.1002/2017GC007026>
- Guillong M, Meyer DL, Allan MM, Heinrich CA, Yardley BWD (2008) SILLS: a Matlab-based program for the reduction of LA-ICP-MS data of homogeneous materials and inclusions. *Mineral Assoc Can Short Course Ser* 40:328–333
- Helmy HM, Ballhaus C, Wohlgemuth-Ueberwasser C, Fonseca ROC, Laurenz V (2010) Partitioning of Se, As, Sb, Te, and Bi between monosulfide solid solution and sulfide melt — application to magmatic sulfide deposits. *Geochim Cosmochim Acta* 74:6174–6179. <https://doi.org/10.1016/j.gca.2010.08.009>
- Horn I, von Blanckenburg F (2007) Investigation on elemental and isotopic fractionation during 196 nm femtosecond laser ablation multiple collector inductively coupled plasma mass spectrometry. *Spectrochim Acta Part B* 62:410–422. <https://doi.org/10.1016/j.sab.2007.03.034>
- Horn I, von Blanckenburg F, Schoenberg R, Steinhofel G, Markl G (2006) In situ iron isotope ratio determination using UV-femtosecond laser ablation with application to hydrothermal ore formation processes. *Geochim Cosmochim Acta* 70:3677–3688. <https://doi.org/10.1016/j.gca.2006.05.002>
- Hu AX, Peng JT (2018) Fluid inclusions and ore precipitation mechanism in the giant Xikuangshan mesothermal antimony deposit, South China: Conventional and infrared microthermometric constraints. *Ore Geol Rev* 95:49–64. <https://doi.org/10.1016/j.oregeorev.2018.02.00>
- Hu J, Gurnis M (2020) Subduction duration and slab dip. *Geochim* 21:e2019GC008862. <https://doi.org/10.1029/2019GC008862>
- Ivan P, Méres Š (2006) Lithostratigraphic division and origin of the Paleozoic part of the crystalline basement of the Malé Karpaty Mts. – a new view based on the results of geochemical research. *Miner Slov* 38:165–186 (in Slovak)
- Jochum KP, Weis U, Stoll B, Kuzmin D, Yang Q, Raczek I, Jacob DE, Stracke A, Birbaum K, Frick DA, Günther D, Enzweiler J (2011) Determination of reference values for NIST SRM 610-617 glasses following ISO guidelines. *Geostand Geoanal Res* 35:397–429. <https://doi.org/10.1111/j.1751-908X.2011.00120.x>
- John T, Gussone N, Podladchikov YY, Bebout GE, Dohmen R, Halama R, Klemd R, Magna T, Seitz H-M (2012) Volcanic arcs fed by rapid pulsed fluid flow through subducting slabs. *Nat Geosci* 5:489–492. <https://doi.org/10.1038/NNGEO1482>
- Kaufmann AB, Lazarov M, Kiefer S, Majzlan J, Weyer S (2021) In situ determination of antimony isotope ratios in Sb minerals by femtosecond LA-MC-ICP-MS. *J Anal At Spectrom* 36:1554–1567. <https://doi.org/10.1039/D1JA00089F>
- Kohút M, Uher P, Putis M, Ondrejka M, Sergeev S, Larionov A, Paderin I (2009) SHRIMP U-Th-Pb zircon dating of the granitoid massifs in the Malé Karpaty Mountains (Western Carpathians): evidence of Meso-Hercynian successive S- to I-type granitic magmatism. *Geol Carpath* 60:345–350. <https://doi.org/10.2478/v10096-009-0026-z>
- Kretschmar U, McBride D (2016) The metallogeny of lode gold deposits: a syngenetic perspective. Elsevier, Amsterdam
- Lazarov M, Horn I (2015) Matrix and energy effects during in-situ determination of Cu isotope ratios by ultraviolet-femtosecond laser ablation multicollector inductively coupled plasma mass spectrometry. *Spectrochim Acta Part B* 111(1):64–73. <https://doi.org/10.1016/j.sab.2015.06.013>
- Li S, Deng Y, Zheng H, Liu X, Tang P, Zhou J, Zhu Z (2021) A new purification method based on a thiol silica column for high precision antimony isotope measurements. *J Anal At Spectrom* 36:157–164. <https://doi.org/10.1039/D0JA00367K>
- Li Y, Audétat A (2012) Partitioning of V, Mn, Co, Ni, Cu, Zn, As, Mo, Ag, Sn, Sb, W, Au, Pb, and Bi between sulfide phases and hydrous basanite melt at upper mantle conditions. *Earth Planet Sci Lett* 355–356:327–340. <https://doi.org/10.1016/j.epsl.2012.08.008>
- Liu J, Chen J, Zhang T, Wang Y, Yuan W, Lang Y, Tu C, Liu L, Birck J-L (2020) Chromatographic purification of antimony for accurate isotope analysis by MC-ICP-MS. *J Anal At Spectrom* 35:1360–1367. <https://doi.org/10.1039/D0JA00136H>
- Lobo L, Devulder V, Degryse P, Vanhaecke F (2012) Investigation of natural isotopic variation of Sb in stibnite ores via multi-collector ICP-mass spectrometry – perspectives for Sb isotopic analysis of Roman glass. *J Anal At Spectrom* 27:1304–1310. <https://doi.org/10.1039/C2JA30062A>
- MacKinney JS (2016) Antimony isotopes as indicators of redox reactions in aqueous systems: fractionation during Sb (V) reduction by sulfide and isotope exchange kinetics between dissolved Sb (III) and Sb (V). Master thesis. University of Illinois
- Majzlan J (2021) Primary and secondary minerals of antimony. In: Filella M (ed) *Antimony*, 1st edn. De Gruyter, Berlin/Boston, pp 17–47. <https://doi.org/10.1515/9783110668711-002>
- Majzlan J, Chovan M, Hurai V, Luptáková J (2020a) Hydrothermal mineralisation of the Tatric Superunit (Western Carpathians,

- Slovakia): I. A review of mineralogical, thermometry and isotope data. *Geol Carpath* 71:85–112. <https://doi.org/10.31577/GeolCarp.71.2.1>
- Majzlan J, Chovan M, Kiefer S, Gerdes A, Kohút M, Siman P, Konečný P, Števkó M, Finger F, Waitzinger M (2020b) Hydrothermal mineralisation of the Tatric Superunit (Western Carpathians, Slovakia): II. Geochronology and timing of mineralisations in the Nízke Tatry Mts. *Geol Carpath* 71:113–133. <https://doi.org/10.31577/GeolCarp.71.2.2>
- Markl G, Blackenburg FV, Wagner T (2006) Iron isotope fractionation during hydrothermal ore deposition and alteration. *Geochim Cosmochim Acta* 70:3011–3030. <https://doi.org/10.1016/j.gca.2006.02.028>
- Mason TFD, Weiss DJ, Chapman JB, Wilkinson JJ, Tessalina SG, Spiro B, Horstwood MSA, Spratt J, Coles BJ (2005) Zn and Cu isotopic variability in the Alexandrinka volcanic-hosted massive sulphide (VHMS) ore deposit, Urals, Russia. *Chem Geol* 221:170–187. <https://doi.org/10.1016/j.chemgeo.2005.04.011>
- Matt P, Peck WH, Mathur R, Hurtgen MR, Godfrey L (2022) Zinc isotope constraints on the formation of sedimentary exhalative (SEDEX) ore deposits: new evidence from the Franklin, NJ mining district. *Ore Geol Rev* 147:104970. <https://doi.org/10.1016/j.oregeorev.2022.104970>
- Moravský D, Lipka J (2004) Phyllosilicates and carbonates from hydrothermally altered metamorphic rocks in the Pezinok Sb–Au deposit, Western Carpathians, Slovakia. *Miner Slov* 36:247–265
- Moussallam Y, Schneider DA, Janák M, Thöni M, Holm DK (2012) Heterogeneous extrusion and exhumation of deep-crustal Variscan assembly: geochronology of the Western Tatra Mountains, northern Slovakia. *Lithos* 144–145:88–108. <https://doi.org/10.1016/j.lithos.2012.03.025>
- Naumov VB, Dorofeeva VA, Mironova OF (2018) Physicochemical parameters of the origin of hydrothermal mineral deposits: evidence from fluid inclusions. V. Antimony, arsenic, and mercury deposits. *Geochem Int* 56:901–914. <https://doi.org/10.1134/S0016702918090082>
- Nevolko PA, Pham TD, Tran TH, Tran TA, Ngo TP, Fominykh PA (2018) Intrusion-related Lang Vai gold-antimony district (Northeastern Vietnam): geology, mineralogy, geochemistry and $^{40}\text{Ar}/^{39}\text{Ar}$ age. *Ore Geol Rev* 96:218–235. <https://doi.org/10.1016/j.oregeorev.2018.04.017>
- Normand C, Gauthier M, Jébrak M (1996) The Québec antimony deposit: an example of gudmundite-native antimony mineralization in the ophiolitic mélange of the southeastern Québec Appalachians. *Econ Geol* 91:149–163. <https://doi.org/10.2113/gsecongeo.91.1.149>
- Olsen NJ, Mountain BW, Seward TM (2018) Antimony (III) sulfide complexes in aqueous solutions at 30°C: a solubility and XAS study. *Chem Geol* 476:233–247. <https://doi.org/10.1016/j.chemgeo.2017.11.020>
- Olsen NJ, Mountain BW, Seward TM (2019) Antimony (III) Speciation in hydrosulfide solutions from 70 to 400°C and up to 300 bar. *ACS Earth Space Chem* 3:1058–1072. <https://doi.org/10.1021/acsearthspacechem.8b00211>
- Patten CGC, Molnár F, Pitcairn IK, Kolb J, Mertanen S, Hector S (2023) Multi-source and multi-stage metal mobilization during the tectonic evolution of the Central Lapland Greenstone Belt, Finland: implications for the formation of orogenic Au deposits. *Miner Deposita* 58:461–488. <https://doi.org/10.1007/s00126-022-01133-z>
- Pitcairn IK, Craw D, Teagle DAH (2015) Metabasalts as sources of metals in orogenic gold deposits. *Miner Deposita* 50:373–390. <https://doi.org/10.1007/s00126-014-0547-y>
- Pitcairn IK, Teagle DAH, Craw D, Olivo GR, Kerrich R, Brewer TS (2006) Sources of metals and fluids in orogenic gold deposits: insights from the Otago and Alpine Schists, New Zealand. *Econ Geol* 101:1525–1546. <https://doi.org/10.2113/gsecongeo.101.8.1525>
- Plašienka D (2018) Continuity and episodicity in the early Alpine tectonic evolution of the Western Carpathians: how large-scale processes are expressed by the orogenic architecture and rock record data. *Tectonics* 37:2029–2079. <https://doi.org/10.1029/2017TC004779>
- Plašienka D, Michalík J, Kováč M, Gross P, Putiš M (1991) Paleotectonic evolution of Malé Karpaty Mts. – an overview. *Geol Carpath* 42:195–208
- Pokrovski GS, Blanchard M, Saunier G, Poitras F (2021) Mechanisms and rates of pyrite formation from hydrothermal fluid revealed by iron isotopes. *Geochimica Cosmochimica Acta* 304:281–304. <https://doi.org/10.1016/j.gca.2006.06.1549>
- Pokrovski GS, Borisova AY, Roux J, Hazemann JL, Petdang A, Tella M, Testemale D (2006) Antimony speciation in saline hydrothermal fluids: a combined X-ray absorption fine structure spectroscopy and solubility study. *Geochim Cosmochim Acta* 70:4196–4214
- Pokrovski GS, Roux J, Harrichoury J-C (2005) Fluid density control on vapor-liquid partitioning of metals in hydrothermal systems. *Geology* 33:657–660. <https://doi.org/10.1130/G21475AR.1>
- Qiu KF, Yu HC, Deng J, McIntire D, Gou ZY, Geng JZ, Chang ZS, Zhu R, Li KN, Goldfarb R (2020) The giant Zaozigou Au-Sb deposit in West Qinling, China: magmatic- or metamorphic-hydrothermal origin? *Miner Deposita* 55:345–362. <https://doi.org/10.1007/s00126-019-00937-w>
- Resongles E, Freydier R, Casiot C, Viers J, Chmieleff J, Elbaz-Poulichet F (2015) Antimony isotopic composition in river waters affected by ancient mining activity. *Talanta* 144:851–861. <https://doi.org/10.1016/j.talanta.2015.07.013>
- Riddley J (2013) *Ore deposit geology*. Cambridge University Press, p 409
- Robb L (2020) *Introduction to ore-forming processes*. Wiley-Blackwell, p 496
- Rouxel O, Ludden J, Fouquet Y (2003) Antimony isotope variations in natural systems and implications for their use as geochemical tracers. *Chem Geol* 200:25–40. [https://doi.org/10.1016/S0009-2541\(03\)00121-9](https://doi.org/10.1016/S0009-2541(03)00121-9)
- Sillitoe RH, Hedenquist JW (2005) Linkages between volcanotectonic settings, ore-fluid compositions, and epithermal precious metal deposits. Special publication, pp 315–343
- Spiridonov EM, Kulagov EA, Serova AA, Kulikova IM, Korotaeva NN, Sereda EV, Tushentsova IN, Belyakov SN, Zhukov NN (2015) Genetic Pd, Pt, Au, Ag, and Rh mineralogy in Noril'sk sulfide ores. *Geol Ore Depos* 57:402–432
- Sun G, Wu Y, Feng X, Wu X, Li X, Deng Q, Wang F, Fu X (2021) Precise analysis of antimony isotopic composition in geochemical materials by MC-ICP-MS. *Chem Geol* 582:120459. <https://doi.org/10.1016/j.chemgeo.2021.120459>
- Tanimizu M, Araki Y, Asaoka S, Takahashi Y (2011) Determination of natural isotopic variation in antimony using inductively coupled plasma mass spectrometry for an uncertainty estimation of the standard atomic weight of antimony. *Geochem J* 45:27–32
- Tossell JA (1994) The speciation of antimony in sulfidic solutions: a theoretical study. *Geochim Cosmochim Acta* 58:5093–5104. [https://doi.org/10.1016/0016-7037\(94\)90296-8](https://doi.org/10.1016/0016-7037(94)90296-8)
- van Haren JLM, Ague JJ, Rye DM (1996) Oxygen isotope record of fluid infiltration and mass transfer during regional metamorphism of pelitic schist, Connecticut, USA. *Geochimica Cosmochimica Acta* 60:3487–3504. [https://doi.org/10.1016/0016-7037\(96\)00182-2](https://doi.org/10.1016/0016-7037(96)00182-2)
- Wang D, Mathur R, Zheng Y, Qiu K, Wu H (2021) Redox-controlled antimony isotope fractionation in the epithermal system: new insights from a multiple metal stable isotopic combination

- study of the Zhaxikang Sb-Pb-Zn-Ag deposit in Southern Tibet. *Chem Geol* 584:120541. <https://doi.org/10.1016/j.chemgeo.2021.120541>
- Wang Y, Zhu XK, Cheng YB (2015) Fe isotope behaviours during sulfide-dominated skarn-type mineralization. *J Asian Earth Sci* 103:374–392. <https://doi.org/10.1016/j.jseaes.2014.11.005>
- Wang Y, Zhu XK, Mao JW, Li ZH, Cheng YB (2011) Iron isotope fractionation during skarn-type metallogeny: a case study of Xinqiao Cu–S–Fe–Au deposit in the Middle–Lower Yangtze valley. *Ore Geol Rev* 43:194–202. <https://doi.org/10.1016/j.oregeorev.2010.12.004>
- Wasserman N, Johnson T, Kulp T (2019) Isotopic fractionation of antimony (Sb) during sorption of Sb(III) and Sb(V) to goethite and illite. *Goldschmidt Conference Abstracts Barcelona*
- Welch SA, Beard BL, Johnson CM, Braterman PS (2003) Kinetic and equilibrium Fe isotope fractionation between aqueous Fe(II) and Fe(III). *Geochim Cosmochim Acta* 67:4231–4250. [https://doi.org/10.1016/S0016-7037\(03\)00266-7](https://doi.org/10.1016/S0016-7037(03)00266-7)
- Wen B, Zhou J, Tang P, Jia X, Zhou W, Huang J (2023) Antimony (Sb) isotopic signature in water systems from the world's largest Sb mine, central China: novel insights to trace Sb source and mobilization. *J Hazard Mater* 446:130622. <https://doi.org/10.1016/j.jhazmat.2022.130622>
- Wen B, Zhou J, Zhou A, Liu C, Li L (2018) A review of antimony (Sb) isotopes analytical methods and application in environmental systems. *Int Biodeterior Biodegrad* 128:109–116. <https://doi.org/10.1016/j.ibiod.2017.01.008>
- Weyer S, Jarick J, Mezger K (1999) Quantitative temperature–time information from retrograde diffusion zoning in garnet: constraints for the P–T–t history of the Central Black Forest, Germany. *J Metamorph Geol* 17:449–461
- Wilkinson JJ, Weiss DJ, Mason TFD, Coles BJ (2005) Zinc isotope variation in hydrothermal systems: preliminary evidence from the Irish midlands ore field. *Econ Geol* 100(3):583–590. <https://doi.org/10.2113/gsecongeo.100.3.583>
- Williams-Jones AE, Normand C (1997) Controls of mineral paragenesis in the system Fe–Sb–S–O. *Econ Geol* 92:308–324. <https://doi.org/10.2113/gsecongeo.92.3.308>
- Xu L, Yang J-H, Zeng Q-D, Xie L-W, Zhu Y-S, Li R, Li B (2020) Pyrite Rb–Sr, Sm–Nd and Fe isotopic constraints on the age and genesis of the Qingchengzi Pb–Zn deposits, northeastern China. *Ore Geol Rev* 117:103324. <https://doi.org/10.1016/j.oregeorev.2020.103324>
- Yu H-C, Qiu K-F, Simon AC, Wang D, Mathur R, Wan R-Q, Jiang X-Y, Deng J (2022) Telescoped boiling and cooling mechanisms triggered hydrothermal stibnite precipitation: insights from the world's largest antimony deposit in Xikuangshan China. *Am Min* 108:1213–1223. <https://doi.org/10.2138/am-2022-8490>
- Zajacz Z, Halter WE, Pettke T, Guillong M (2008) Determination of fluid/melt partition coefficients by LA-ICPMS analysis of co-existing fluid and silicate melt inclusions: controls on element partitioning. *Geochim Cosmochim Acta* 72:2169–2197. <https://doi.org/10.1016/j.gca.2008.01.034>
- Zhai D, Mathur R, Liu SA, Liu J, Godfrey L, Wang K, Vervoort J (2021) Antimony isotope fractionation in hydrothermal systems. *Geochim Cosmochim Acta* 12215. <https://doi.org/10.1016/j.gca.2021.05.031>
- Zhao Y, Liu S-A, Xue C, Li M-L (2022) Copper isotope evidence for a Cu-rich mantle source of the world-class Jinchuan magmatic Ni–Cu deposit. *Am Min* 107:673–683. <https://doi.org/10.2138/am-2021-7911>
- Zhou W, Zhou A, Wen B, Liu P, Zhu Z, Finckel Z, Zhou J (2022) Antimony isotope fractionation during adsorption on aluminum oxides. *J Hazard Mater* 429:128317. <https://doi.org/10.1016/j.jhazmat.2022.128317>
- Zhou W, Zhou J, Feng X, Wen B, Zhou A, Liu P, Sun G, Zhou Z, Liu X (2023) Antimony isotope fractionation revealed from EXAFS during adsorption on Fe (oxyhydr)oxides. *Environ Sci Technol* 57:9353–9361. <https://doi.org/10.1021/acs.est.3c01906>
- Zotov AV, Shikina ND, Akinfiev NN (2003) Thermodynamic properties of the Sb (III) hydroxide complex $\text{Sb}(\text{OH})_3(\text{aq})$ at hydrothermal conditions. *Geochim Cosmochim Acta* 67:1821–1836. [https://doi.org/10.1016/S0016-7037\(02\)01281-4](https://doi.org/10.1016/S0016-7037(02)01281-4)

Publisher's Note Springer Nature remains neutral with regard to jurisdictional claims in published maps and institutional affiliations.